CrossMark

J. Fluid Mech. (2018), *vol.* 848, *pp.* 906–945. © Cambridge University Press 2018
doi:10.1017/jfm.2018.358

Faraday instability and subthreshold Faraday waves: surface waves emitted by walkers

Loïc Tadrist[1,†], Jeong-Bo Shim[2], Tristan Gilet[1] and Peter Schlagheck[2]

[1]Microfluidics Lab, Department of Mechanical and Aerospace Engineering, University of Liege, Allée de la découverte 9, 4000 Liège, Belgium

[2]IPNAS, CESAM research unit, University of Liege, Allee du 6 Août 15, 4000 Liège, Belgium

(Received 16 November 2017; revised 12 March 2018; accepted 24 April 2018; first published online 13 June 2018)

A walker is a fluid entity comprising a bouncing droplet coupled to the waves that it generates at the surface of a vibrated bath. Thanks to this coupling, walkers exhibit a series of wave–particle features formerly thought to be exclusive to the quantum realm. In this paper, we derive a model of the Faraday surface waves generated by an impact upon a vertically vibrated liquid surface. We then particularise this theoretical framework to the case of forcing slightly below the Faraday instability threshold. Among others, this theory yields a rationale for the cosine dependence of the wave amplitude to the phase shift between impact and forcing, as well as the characteristic time scale and length scale of viscous damping. The theory is validated with experiments of bead impact on a vibrated bath. We finally discuss implications of these results for the analogy between walkers and quantum particles.

Key words: Faraday waves, parametric instability, waves/free-surface flows

1. Introduction

Michael Faraday (1831) gave a first experimental description of the instability that would be named after him. The Faraday instability occurs when a container filled with liquid is vertically vibrated with an acceleration $\Gamma g \cos(\Omega t)$, where g is the gravitational acceleration and $\Omega/2\pi$ is the shaking frequency. When the dimensionless amplitude Γ is higher than a threshold Γ_F, the forcing is sufficient to counterbalance viscous dissipation (Kumar & Tuckerman 1994), the initially flat free surface destabilises and beautiful patterns of standing waves spontaneously appear. The resonance is often subharmonic so the frequency of the standing waves is $\Omega/4\pi$. The Faraday wavelength λ_F, defined as the characteristic wavelength of the standing waves, is usually close to the wavelength prescribed by the dispersion relation of gravity–capillary waves with a frequency $\Omega/4\pi$. In its original and now most studied configuration (Benjamin & Ursell 1954), the depth and lateral extension of the liquid bath are respectively much deeper and much larger than the wavelength, which ensures that the resonance is subharmonic.

Below the Faraday instability threshold, all surface waves are damped and, without any perturbation, the liquid surface remains flat. A perturbation can be added in

† Email address for correspondence: Loic.tadrist@uliege.be

https://doi.org/10.1017/jfm.2018.358 Published online by Cambridge University Press

the form of a bouncing droplet. If the vertical vibration of the bath is of sufficient amplitude, this droplet can bounce on the bath periodically and indefinitely (Couder *et al.* 2005*a*; Gilet *et al.* 2008; Molacek & Bush 2013). Couder *et al.* (2005*b*) showed that such droplets may excite Faraday waves, especially if they can bounce once every two forcing periods (i.e. at frequency $\Omega/4\pi$). If the forcing amplitude is slightly below the instability threshold ($\Gamma \lesssim \Gamma_F$), these waves are slowly damped and they are still present when the droplet impacts again (Eddi *et al.* 2011). Consequently, the droplet impacts on a non-flat surface and some horizontal momentum can be transferred from the wave to the droplet. The latter starts to 'walk' on the vibrated liquid surface. The combination of a walking droplet and the underlying surface waves is called a walker. A typical walker involves a droplet of radius $R_d = 0.4$ mm and a bath of depth 6 mm, both made of silicone oil of density $\rho = 956$ kg m^{-3}, kinematic viscosity $\nu = 20$ cS and surface tension $\sigma = 20.6$ mN m^{-1}. The bath is typically shaken at a frequency $\Omega/(2\pi) = 80$ Hz with an amplitude $\Gamma \sim 4$ (table 1).

Walkers form a unique macroscopic analogue of the pilot-wave theory imagined by de Broglie (1987) as an interpretation of quantum mechanics. In a series of configurations recently summarised by Bush (2015), the behaviour of walkers is strongly reminiscent of that of quantum particles. Quantisation of bound states is observed in a central force field (Perrard *et al.* 2014*a*,*b*; Labousse *et al.* 2014, 2016; Tambasco *et al.* 2016), in a rotating frame (Fort *et al.* 2010; Eddi *et al.* 2012; Harris & Bush 2014; Oza *et al.* 2014*a*,*b*), or with two-body interactions (Protiere, Boudaoud & Couder 2006; Protière, Bohn & Couder 2008; Borghesi *et al.* 2014; Filoux, Hubert & Vandewalle 2015; Durey & Milewski 2017; Oza *et al.* 2017). Walkers interact with submerged boundaries through non-specular reflection (Pucci *et al.* 2016) and tunnelling (Eddi *et al.* 2009; Carmigniani *et al.* 2014; Nachbin, Milewski & Bush 2017). More remarkably, when they are confined in a cavity, they experience chaotic trajectories for which the corresponding statistics is close to the quantum statistics predicted by the Schrödinger equation (Harris *et al.* 2013; Gilet 2014, 2016). They also seem to be diffracted when they pass one by one above a submerged slit (Couder & Fort 2006, 2012; Dubertrand *et al.* 2016), although it is not yet clear that the underlying statistics is really similar to that of a diffracted quantum particle (Andersen *et al.* 2015). Walkers therefore represent a unique opportunity to probe the boundary between the macroscopic world and the quantum realm. They allow us to identify which specific behaviours of quantum particles could be explained or not through the deterministic coupling of a wave and a particle.

An appropriate model of the damped Faraday waves emitted by the bouncing droplet is necessary to rationalise the dynamics of walkers. The first model has been proposed by Benjamin & Ursell (1954) for an inviscid fluid. Since there is no dissipation, the instability threshold is then identically zero. The Navier–Stokes equations simplify into a Matthieu equation for the interface elevation $\zeta(x, y, t)$. In the limit of infinite depth, it reads

$$\frac{\mathrm{d}^2\zeta}{\mathrm{d}t^2} + \left[gk + \frac{\sigma}{\rho}k^3 - \Gamma gk\cos(\Omega t)\right]\zeta = 0, \tag{1.1}$$

where k is the wavenumber. There is a subharmonic resonance for the Faraday wavenumber $k_F = 2\pi/\lambda_F$ such that:

$$\frac{\Omega^2}{4} = gk_F + \frac{\sigma}{\rho}k_F^3. \tag{1.2}$$

https://doi.org/10.1017/jfm.2018.358 Published online by Cambridge University Press

https://doi.org/10.1017/jfm.2018.358 Published online by Cambridge University Press

General parameters							
Three-dimensional vector position	$\boldsymbol{r} = (x, y, z)$			Two-dimensional vector position	$\boldsymbol{r} = (x, y)$		
Radial distance	r			Time	t		
Dimensionless time	$\tau = \Omega t/2$			Laplace variable	s		
Wavelength	λ			Wavenumber	k		
Fields							
Pressure field	$P(\boldsymbol{r}, t)$			Velocity field	$\boldsymbol{v}(\boldsymbol{r}, t)$		
Vertical velocity	$v_z(\boldsymbol{r}, t)$			Surface wave profile	$\zeta(\boldsymbol{r}, t)$		
Fluid parameters							
Gravity acceleration	g	9.81	m s^2	Density	ρ	956	kg m^{-3}
Surface tension	σ	20.6	mN m^{-1}	Viscosity	ν	20	cS
Input parameters							
Shaker pulsation	Ω	$2\pi \times 80$	m^{-1}	Driving strength	Γ		
Walking velocity	V_w	11	mm s^{-1}	reduced form, υ	$2V_w/\Omega$	43.8	μm
Impact phase	τ_i						
Output parameters							
Faraday period	T_F	25	ms	Faraday threshold	Γ_F	4.155	
Faraday wavelength	λ_F	4.749	mm	Faraday wavenumber	k_F	1323	m^{-1}
Phase shift	θ_F	$\pi/4$		Damping length	l	10.2	mm
Damping time	$1/\delta_F$	−49		dimensional form	$2/\Omega\delta_F$	195	ms
Diffusion coefficient	D	2.20	mm^2	dimensional form	$\Omega D/2$	5.5	cm^2 s^{-1}
Group velocity	c_F	0.983	mm	dimensional form	$\Omega c_F/2$	24.7	cm s^{-1}
Dimensionless parameters							
Free pulsation	ω_0	1		Free damping	γ_0	0.2771	
Threshold distance	$\mathcal{M}$	10		Memory number	Me	7.65	

TABLE 1. Table of notations used in the paper. Subscript $_0$ (respectively $_F$ and $_i$) refers to the solution for a null viscosity (respectively to the solution at the Faraday threshold and to the quantities relative to the impact).

In order to account for a finite viscosity ν, a phenomenological linear damping term is added to this Matthieu equation (e.g. Kumar & Tuckerman (1994), Eddi *et al.* (2011), Moláček & Bush (2013), Blanchette (2016)):

$$\frac{\mathrm{d}^2\zeta}{\mathrm{d}t^2} + 2\alpha\nu k^2\frac{\mathrm{d}\zeta}{\mathrm{d}t} + \left[gk + \frac{\sigma}{\rho}k^3 - \Gamma gk\cos(\Omega t)\right]\zeta = 0, \tag{1.3}$$

where α is a dimensionless factor. A slightly different model is derived by Milewski *et al.* (2015) from the Navier–Stokes equations in the limit of small viscosity, without any additional phenomenological term (Durey & Milewski 2017):

$$\frac{\mathrm{d}^2\zeta}{\mathrm{d}t^2} + 4\nu k^2\frac{\mathrm{d}\zeta}{\mathrm{d}t} + \left[gk + \frac{\sigma}{\rho}k^3 + 4\nu^2k^4 - \Gamma gk\cos(\Omega t)\right]\zeta = 0. \tag{1.4}$$

The wave field generated by one impact of the bouncing droplet at position $\boldsymbol{r}_n$ at time t_n is then approximately (Moláček & Bush 2013; Milewski *et al.* 2015)

$$\zeta_1(\boldsymbol{r}-\boldsymbol{r}_n, t-t_n) = \frac{A\sin\Phi}{\sqrt{t-t_n}}\mathrm{J}_0(k_F|\boldsymbol{r}-\boldsymbol{r}_n|)\exp\left(-\frac{\Omega(t-t_n)}{4\pi Me}\right)\cos\left(\frac{\Omega t}{2}\right), \tag{1.5}$$

where $Me = \Omega\Gamma_F/[(8\pi\nu k_F^2)(\Gamma_F - \Gamma)]$ is defined as the memory parameter, A is a constant amplitude that represents the strength of the impact and Φ is linked (but not strictly equal) to the impact phase relative to the shaker. In the presence of obstacles, this equation (1.5) can be replaced by a more elaborate Green's function that takes the wave reflection on boundaries into account (Dubertrand *et al.* 2016). It has also been suggested in Fort *et al.* (2010), Eddi *et al.* (2011) to add a spatial damping factor $\mathrm{e}^{-|\boldsymbol{r}-\boldsymbol{r}_n|/l}$, where $l \sim 1.6\lambda_F$ is a characteristic damping length.

The wave field generated by a walker is assumed linear, so it can be computed by summing wave contributions from successive impacts:

$$\zeta(\boldsymbol{r}, t) = \sum_n \zeta_1(\boldsymbol{r}-\boldsymbol{r}_n, t-t_n). \tag{1.6}$$

A walker that does not experience any interaction with either boundaries or other walkers, moves at constant horizontal speed and impacts the bath at regular times $t_n = t_i + 4\pi n/\Omega$. This is referred as the 'stroboscopic approximation' and it is implemented in all currently existing models of walkers, with the recent exception of that of Oza *et al.* (2017). Some models assume an instantaneous interaction of the droplet with the bath for the sake of simplicity (Eddi *et al.* 2011; Gilet 2016; Durey & Milewski 2017), whereas more sophisticated models take into account a finite time of interaction of the droplet with the bath at each impact (Moláček & Bush 2013; Milewski *et al.* 2015). When the 'stroboscopic approximation' is combined with the additional assumption that the horizontal translation of the walker during one rebound is much less than the Faraday wavelength λ_F, the sum of impacts can be replaced by a time integral, which yields an integro-differential equation for the walker trajectory (Oza, Rosales & Bush 2013; Bush, Oza & Moláček 2014).

There are several issues with (1.5) and its variants. First, the elevation ζ of waves created by a single impact diverges in $t \to t_n$, which is unphysical. Second, the viscosity is taken into account through the damping factor α and the spatial damping length l, both of which are empirical corrections assumed to be valid only when

https://doi.org/10.1017/jfm.2018.358 Published online by Cambridge University Press

viscous damping is weak. However, for the typical experimental conditions described above, the damping time $1/(4\nu k_F^2) \sim 0.007$ s is actually smaller than the Faraday period $4\pi/\Omega = 0.025$ s. So viscous damping is definitely not weak, and one needs to check how much error is made by using these low-viscosity empirical approximations. Third, Faraday waves are assumed in phase with the forcing signal, and of constant amplitude A, without any proof or experimental evidence. The dependence of A to the phase shift between the impact and the forcing signal has never been evidenced experimentally.

Without perturbations, a walker moves horizontally along a straight line, with a perfectly periodic bouncing motion. Therefore, these three limitations of (1.5) may induce discrepancies between models and experiments as soon as the walker's bouncing is perturbed, either by the presence of boundaries, other walkers or waves that it left previously. Indeed, there is then no guarantee that the bouncing motion will remain periodic, and any perturbation of the impact phase would induce a different weight of each rebound to the wave field. This weight is also strongly dependent on temporal and spatial damping factors. The latter basically defines the distance below which a significant interaction between multiple walkers is expected. A wave field constructed with different weights for each impact will necessarily be qualitatively different, and so will the resulting walker trajectory be. The aforementioned perturbations by boundaries, other walkers and self-interferences, all correspond to configurations where quantum-like phenomena were observed. They seem to be key to the analogy between walkers and quantum particles.

The main aim of this article is to obtain a quantitatively more accurate understanding of the surface waves emitted by walkers. The Faraday instability has been the subject of much theoretical work since Benjamin & Ursell (1954). Most notably, Kumar & Tuckerman (1994) solved the full linearised Navier–Stokes equations (without any assumption on viscosity or depth) with a spectral method based on Floquet's theory. They showed, by comparing curves of marginal stability, that the damped Matthieu equation (1.3) misses an important additional dissipation in the boundary layer at the liquid/air interface that only the full model can capture. However, because of the parametric forcing, the harmonics of the Floquet series are coupled to each other. Consequently, the dispersion relation can only be obtained by solving a discouraging eigenvalue problem for a matrix of infinite dimension.

The truncation of the Floquet series of Kumar & Tuckerman (1994) to four harmonics ($\pm\Omega/2$ and $\pm 3\Omega/2$) has been investigated by Kumar (1996). With this truncated model, they could show that right above the threshold ($\Gamma \gtrsim \Gamma_F$), Faraday waves are always subharmonic when both the depth h and the Faraday wavelength λ_F are much larger than the size of the boundary layer $\sqrt{2\nu/\Omega}$. This is the case for walkers since $\sqrt{2\nu/\Omega} \simeq 300$ μm $\ll h \simeq 6$ mm and $\lambda_F \simeq 4.7$ mm. Special wave patterns, including solitons, appear at the bicritical point where the boundary layer thickness is of the same order of magnitude as either the depth h or the wavelength λ_F (Lioubashevski, Arbell & Fineberg 1996; Wagner, Müller & Knorr 2003). An extreme truncation to only the subharmonic response $\pm\Omega/2$ has been performed by Beyer & Friedrich (1995) as well as Müller *et al.* (1997). Müller *et al.* (1997) could then derive an analytical expression for the Faraday threshold Γ_F in the limit of low viscosity (i.e. $\nu k^2/\Omega \ll 1$) and large depth.

In this paper, we follow the approach of Müller *et al.* (1997) to describe the Faraday waves emitted by walkers. In § 2, we first derive an analytical model of slightly damped Faraday waves, while keeping control on the approximations that are made (e.g. the approximation of low viscosity). We then calculate the wave field

https://doi.org/10.1017/jfm.2018.358 Published online by Cambridge University Press

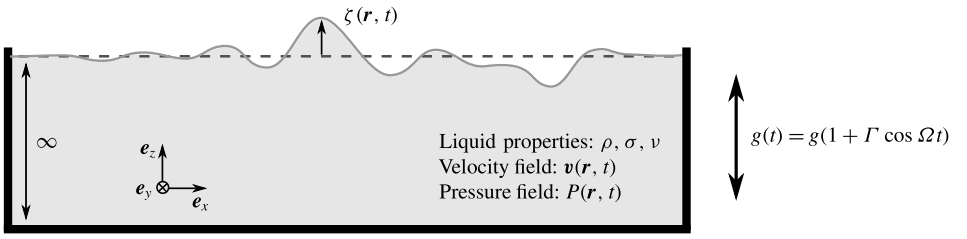


FIGURE 1. A liquid bath of infinite depth is vibrated vertically. The liquid experiences a time varying effective gravity $g(t)$. The elevation of the liquid surface is denoted $\zeta(x, y, t) = \zeta(\boldsymbol{r}, t)$. The velocity and pressure fields inside the liquid bath are $\boldsymbol{v}(\boldsymbol{r}, t)$ and $P(\boldsymbol{r}, t)$, respectively.

generated by a series of impacts. In § 3, we report the results of experiments on Faraday waves excited by an impacting bead. We show that our model goes beyond the identified limitations of (1.5) currently used to describe walkers. In § 4, we finally discuss the implication of this wave model for the development of the analogy between walkers and quantum particles.

2. Surface wave theory for walkers

2.1. *The surface wave equation*

We consider an infinitely extended and infinitely deep Newtonian liquid with density ρ, surface tension σ and viscosity ν (figure 1). This liquid is incompressible, i.e. $\boldsymbol{\nabla} \cdot \boldsymbol{v}(\boldsymbol{r}, t) = 0$, where $\boldsymbol{v}$ is the velocity field within the liquid. It is subjected to a periodic vertical vibration of frequency Ω and acceleration amplitude Γg, where $g = 9.81$ m s^{-2} is the gravitational acceleration. Within the comoving frame, the liquid is then effectively experiencing a time-periodic modulation of gravity according to

$$g(t) = g[1 + \Gamma \cos(\Omega t)]. \tag{2.1}$$

The spatio-temporal evolution of the liquid is governed by the Navier–Stokes equation,

$$\frac{\partial}{\partial t}\boldsymbol{v}(\boldsymbol{r}, t) + (\boldsymbol{v}(\boldsymbol{r}, t) \cdot \boldsymbol{\nabla})\boldsymbol{v}(\boldsymbol{r}, t) = -\frac{1}{\rho}\boldsymbol{\nabla} P(\boldsymbol{r}, t) - g(t)\boldsymbol{e}_z + \nu \boldsymbol{\nabla}^2 \boldsymbol{v}(\boldsymbol{r}, t), \tag{2.2}$$

where $\boldsymbol{r} = [x, y, z]$ and $P(\boldsymbol{r}, t)$ denotes the pressure within the liquid relative to the atmospheric pressure. Without loss of generality, we choose a coordinate system whose origin is located at the surface of the liquid at rest, with the z-axis oriented upwards (i.e. opposite to the direction of the gravitational force). We consider small deviations from the stationary equilibrium state $\boldsymbol{v}^{(eq)}(\boldsymbol{r}, t) = 0$ and $P^{(eq)}(\boldsymbol{r}, t) = -\rho g(t) z$ of the liquid. Under the assumption that the amplitude of the resulting elevation ζ of the free surface is much smaller than both the thickness of the viscous boundary layer $\sqrt{2\nu/\Omega}$ and the Faraday wavelength λ, we may linearise the Navier–Stokes equation (2.2):

$$\frac{\partial}{\partial t}\boldsymbol{v}(\boldsymbol{r}, t) - \nu \boldsymbol{\nabla}^2 \boldsymbol{v}(\boldsymbol{r}, t) = -\frac{1}{\rho}\boldsymbol{\nabla} p(\boldsymbol{r}, t), \tag{2.3}$$

https://doi.org/10.1017/jfm.2018.358 Published online by Cambridge University Press

where $p(\boldsymbol{r}, t) = P(\boldsymbol{r}, t) + \rho g(t) z$ denotes the pressure perturbation. As discussed in appendix F, the conditions of linearisation are satisfied for experimental realisations of walkers. Indeed, the measured wave amplitude is smaller than 12 μm (Damiano *et al.* 2016), which is at least one order of magnitude smaller than both the thickness of the viscous boundary layer (∼300 μm) and the Faraday wavelength (∼4.7 mm). Owing to the incompressibility of the liquid, p satisfies the Laplace equation $\nabla^2 p(\boldsymbol{r}, t) = 0$.

The boundary conditions at the surface $z = 0$ of the liquid are also obtained under the assumption that the liquid is only weakly perturbed: the wave amplitude is assumed much smaller than both the characteristic wavelength and the boundary layer thickness. The absence of tangential shear stress at the surface can then be expressed as

$$\frac{\partial v_z}{\partial u}(x, y, 0, t) + \frac{\partial v_u}{\partial z}(x, y, 0, t) = 0, \tag{2.4}$$

with $u = x$ or y, which together with the incompressibility condition yields the boundary condition

$$\frac{\partial^2 v_z}{\partial z^2}(x, y, 0, t) = \left(\frac{\partial^2}{\partial x^2} + \frac{\partial^2}{\partial y^2}\right) v_z(x, y, 0, t) \tag{2.5}$$

for the vertical component of the liquid velocity. The pressure, on the other hand, satisfies the boundary condition

$$P(x, y, 0, t) = 2\nu\rho \frac{\partial v_z}{\partial z}(x, y, 0, t) - \sigma \left(\frac{\partial^2}{\partial x^2} + \frac{\partial^2}{\partial y^2}\right) \zeta(x, y, t) + P^{ext}(x, y, t), \tag{2.6}$$

at the surface of the liquid. Here $\zeta(x, y, t)$ denotes the surface wave profile, i.e. the local elevation of the surface with respect to the equilibrium level $z = 0$. It satisfies the kinematic condition

$$\frac{\partial}{\partial t}\zeta(x, y, t) = v_z(x, y, 0, t). \tag{2.7}$$

The pressure $P^{ext}(x, y, t)$ represents the spatio-temporal pressure profile that is induced from above the liquid, e.g. by the impact of a droplet on the surface (Milewski *et al.* 2015). This gives rise to the boundary condition

$$\begin{aligned} p(x, y, 0, t) \;=\; & 2\nu\rho \frac{\partial v_z}{\partial z}(x, y, 0, t) - \sigma \left(\frac{\partial^2}{\partial x^2} + \frac{\partial^2}{\partial y^2}\right) \zeta(x, y, t) + \rho g(t) \zeta(x, y, t) \\ & + P^{ext}(x, y, t) \end{aligned} \tag{2.8}$$

for the local pressure perturbation.

Since the lateral extension of the bath is here supposed infinite, the above equations can be simplified by means of a Fourier ansatz defined through

$$X(x, y, z, t) = \frac{1}{2\pi} \int \mathrm{d}k_x \, \mathrm{d}k_y X_{\boldsymbol{k}}(z, t) \exp[\mathrm{i}(k_x x + k_y y)], \tag{2.9}$$

where X is any of the variables ζ, p, v_z or P^{ext}, and where the horizontal wave vector $\boldsymbol{k} = (k_x, k_y)$. Defining $k = |\boldsymbol{k}|$, the Laplace equation for the pressure perturbation is then expressed as

$$\left(\frac{\partial^2}{\partial z^2} - k^2\right) p_{\boldsymbol{k}}(z, t) = 0. \tag{2.10}$$

https://doi.org/10.1017/jfm.2018.358 Published online by Cambridge University Press

This equation is straightforwardly solved as $p_k(z,\,t) = p_k(0,\,t)\mathrm{e}^{kz}$ using the boundary conditions

$$p_k(0,\,t) = 2\nu\rho\frac{\partial v_{z,k}}{\partial z}(0,\,t) + [\rho g(t) + \sigma k^2]\zeta_k(t) + P_k^{ext}(t) \quad \text{and} \quad p_k(-\infty,\,t) = 0. \tag{2.11a,b}$$

The Fourier transform of the linearised Navier–Stokes equation (2.3) then yields

$$\left(\frac{\partial}{\partial t} - \nu\frac{\partial^2}{\partial z^2} + \nu k^2\right) v_{z,k}(z,\,t) \;=\; -\left\{2\nu\frac{\partial v_{z,k}}{\partial z}(0,\,t) + \left[g(t) + \frac{\sigma}{\rho}k^2\right]\zeta_k(t)\right\} k\mathrm{e}^{kz} - \frac{k}{\rho}P_k^{ext}(t)\mathrm{e}^{kz}, \tag{2.12}$$

with boundary conditions

$$\frac{\partial}{\partial t}\zeta_k(t) = v_{z,k}(0,\,t) \tag{2.13}$$

and

$$\frac{\partial^2 v_{z,k}}{\partial z^2}(0,\,t) = -k^2 v_{z,k}(0,\,t). \tag{2.14}$$

We now normalise the main variables with the characteristic time scale $2/\Omega$, and we define:

$$\tau = \frac{\Omega}{2}t, \quad w_k = \frac{2}{\Omega}v_{z,k}, \quad \Pi_k = \frac{4k}{\Omega^2\rho}P_k^{ext}, \quad \gamma_k = \frac{4\nu k^2}{\Omega} \quad \text{and} \quad \omega_k^2 = \frac{4(gk + (\sigma/\rho)k^3)}{\Omega^2}. \tag{2.15a–e}$$

With this set of notations, equations (2.12)–(2.14) become,

$$\left.\begin{gathered}\left(\frac{\partial}{\partial\tau} - \frac{\gamma_k}{2k^2}\frac{\partial^2}{\partial z^2} + \frac{\gamma_k}{2}\right) w_k(z,\,\tau) = -\left\{\frac{\gamma_k}{k}\frac{\partial w_k}{\partial z}(0,\,\tau) + \left[\omega_k^2 + \frac{4\Gamma gk}{\Omega^2}\cos(2\tau)\right]\zeta_k(\tau)\right\}\mathrm{e}^{kz} \\ -\Pi_k(\tau)\mathrm{e}^{kz}, \\ \frac{\partial}{\partial\tau}\zeta_k(\tau) = w_k(0,\,\tau) \quad \text{and} \quad \frac{\partial^2 w_k}{\partial z^2}(0,\,\tau) = -k^2 w_k(0,\,\tau).\end{gathered}\right\} \tag{2.16}$$

We now define the Laplace transform on the dimensionless time τ with zero initial condition (bath surface at rest),

$$w_{k,s}(z) = \int_0^\infty w_k(z,\,\tau)\mathrm{e}^{-s\tau}\,\mathrm{d}\tau \tag{2.17}$$

and apply it to the three equations (2.16):

$$\left.\begin{gathered}\left(s - \frac{\gamma_k}{2k^2}\frac{\partial^2}{\partial z^2} + \frac{\gamma_k}{2}\right) w_{k,s}(z) = -\left\{\frac{\gamma_k}{k}\frac{\partial w_{k,s}}{\partial z}(0) + \omega_k^2\zeta_{k,s} + \frac{2\Gamma gk}{\Omega^2}(\zeta_{k,s+2\mathrm{i}} + \zeta_{k,s-2\mathrm{i}})\right\}\mathrm{e}^{kz} \\ -\Pi_{k,s}\mathrm{e}^{kz}, \\ s\zeta_{k,s} = w_{k,s}(0) \quad \text{and} \quad \frac{\partial^2 w_{k,s}}{\partial z^2}(0) = -k^2 w_{k,s}(0).\end{gathered}\right\} \tag{2.18}$$

https://doi.org/10.1017/jfm.2018.358 Published online by Cambridge University Press

The solution to the above differential equation can be expressed as

$$w_{\boldsymbol{k},s} = [-\gamma_k \mathrm{e}^{\sqrt{1+2s/\gamma_k}kz} + (s+\gamma_k)\mathrm{e}^{kz}]\zeta_{\boldsymbol{k},s}, \tag{2.19}$$

provided that $\zeta_{\boldsymbol{k},s}$ satisfies the relation

$$f_k(s)\zeta_{\boldsymbol{k},s} + \frac{2\Gamma gk}{\Omega^2}(\zeta_{\boldsymbol{k},s+2\mathrm{i}} + \zeta_{\boldsymbol{k},s-2\mathrm{i}}) + \Pi_{\boldsymbol{k},s} = 0, \tag{2.20}$$

where we define the function

$$f_k(s) = (s+\gamma_k)^2 - \gamma_k^{3/2}\sqrt{\gamma_k + 2s} + \omega_k^2. \tag{2.21}$$

This function and all its derivatives are self-conjugated, i.e. $f_k(z^*) = (f_k(z))^*$. Similarly to Müller *et al.* (1997), we finally obtain the equation for surface waves of a shaken bath in the time domain, by back Laplace transforming the previous equation,

$$\left[\frac{\partial^2 \cdot}{\partial \tau^2} + 2\gamma_k \frac{\partial \cdot}{\partial \tau} + \gamma_k^2 + \omega_k^2\right]\zeta_{\boldsymbol{k}}(\tau) - \frac{\gamma_k^{3/2}}{\sqrt{2\pi}}\int_{-\infty}^{\tau} \frac{\mathrm{e}^{-\gamma_k(\tau-u)/2}}{\sqrt{\tau-u}}\left(\gamma_k\zeta_{\boldsymbol{k}}(u) + 2\frac{\partial \zeta_{\boldsymbol{k}}}{\partial u}(u)\right)\mathrm{d}u$$
$$+ \frac{4\Gamma gk}{\Omega^2}\cos(2\tau)\zeta_{\boldsymbol{k}}(\tau) + \Pi_{\boldsymbol{k}}(\tau) = 0, \tag{2.22}$$

given that $\mathcal{L}^{-1}\{1/\sqrt{\gamma_k + 2s}\} = \mathrm{e}^{-\gamma_k\tau/2}/\sqrt{2\pi\tau}$. Equation (2.22) can be integrated numerically to obtain the time dependency of each Fourier component k of the surface wave elevation. Several terms of this equation are identical to terms of the equation (1.4) obtained by Milewski *et al.* (2015) in the limit of low viscosity. However, the convolution integral in (2.22), which is an additional signature of viscous shear, is missing in (1.4).

2.1.1. *Waves on an unshaken bath in the absence of external perturbation*

In the absence of any external perturbation of the liquid (i.e. for $\Gamma = 0$ and $\Pi_{\boldsymbol{k},s} = 0$ for all $\boldsymbol{k}$), the surface wave equation (2.20) becomes $f_k(s)\zeta_{\boldsymbol{k},s} = 0$. The condition of existence of waves $\zeta_{\boldsymbol{k},s} \neq 0$ leads to the dispersion relation of free viscous gravity–capillary waves:

$$f_k(s) = (s+\gamma_k)^2 - \gamma_k^{3/2}\sqrt{\gamma_k + 2s} + \omega_k^2 = 0. \tag{2.23}$$

Equation (2.23) can be solved for s in the low-viscosity limit $\gamma_k \ll 1$:

$$\mathrm{Re}(s) = -\gamma_k\left\{1 - \frac{1}{2}\left(\frac{\gamma_k}{\omega_k}\right)^{1/2} - \frac{1}{8}\left(\frac{\gamma_k}{\omega_k}\right)^{3/2} - \frac{1}{64}\left(\frac{\gamma_k}{\omega_k}\right)^{5/2} + O\left(\left(\frac{\gamma_k}{\omega_k}\right)^{9/2}\right)\right\}, \tag{2.24}$$

$$\mathrm{Im}(s) = \omega_k\left\{1 - \frac{1}{2}\left(\frac{\gamma_k}{\omega_k}\right)^{3/2} + \frac{1}{8}\left(\frac{\gamma_k}{\omega_k}\right)^{5/2} - \frac{1}{64}\left(\frac{\gamma_k}{\omega_k}\right)^{7/2} + \frac{1}{8}\left(\frac{\gamma_k}{\omega_k}\right)^{4} + O\left(\left(\frac{\gamma_k}{\omega_k}\right)^{9/2}\right)\right\}, \tag{2.25}$$

where $\mathrm{Re}(s)$ and $\mathrm{Im}(s)$ represent respectively the damping and the frequency of the waves. The coefficients γ_k and ω_k therefore correspond to the first-order damping and frequency of gravity–capillary waves in the limit of low viscosity.

https://doi.org/10.1017/jfm.2018.358 Published online by Cambridge University Press

2.2. *Faraday waves, just below the Faraday threshold*

We now consider Faraday waves on a bath that is shaken just below the Faraday threshold Γ_F, i.e. in the conditions experienced by walkers. The goal of this section is to determine the damping and the phase shift of these waves. When they are subharmonic (as observed experimentally), they can be obtained by solving (2.22) with the Floquet ansatz

$$\zeta_k(t) = \sum_{l=-\infty}^{\infty} \zeta_k^{(l)} \mathrm{e}^{(2l-1)\mathrm{i}\tau} \mathrm{e}^{\delta_k \tau}, \tag{2.26}$$

where δ_k is a small complex perturbation from the subharmonic resonance frequency that should vanish when the instability threshold is reached. Equivalently in the Laplace domain,

$$\zeta_{k,s} = \sum_{l=-\infty}^{\infty} \frac{\zeta_k^{(l)}}{s + \mathrm{i}(1-2l) - \delta_k}. \tag{2.27}$$

Obtaining the exact solution to (2.20) from this ansatz requires solving an infinite system of algebraic equations where all the Floquet components $\zeta_k^{(l)}$ are coupled to each other (Kumar & Tuckerman 1994). As already suggested by Müller *et al.* (1997), we can simplify this ansatz by restricting it to the two most relevant Floquet components $\zeta_k^{(0)}$ and $\zeta_k^{(1)}$ of the wave, namely those that are associated with angular frequencies in the vicinity of $\pm\Omega/2$. This truncated Floquet ansatz can be written as

$$\left.\begin{aligned} \zeta_k(\tau) &\simeq (\zeta_k^{(1)} \mathrm{e}^{\mathrm{i}\tau} + \zeta_k^{(0)} \mathrm{e}^{-\mathrm{i}\tau}) \mathrm{e}^{\delta_k \tau}, \\ \zeta_{k,s} &\simeq \frac{\zeta_k^{(1)}}{s - \mathrm{i} - \delta_k} + \frac{\zeta_k^{(0)}}{s + \mathrm{i} - \delta_k}. \end{aligned}\right\} \tag{2.28}$$

It is shown in appendix A that this truncation to the two first terms is valid as long as $|f_k(\mathrm{i})|^2/|f_k(3\mathrm{i})|^2 \ll 1$, which is true for wavenumbers $k \sim k_F$ in the low-viscosity limit.

In the absence of external pressure applied on the bath, $\Pi_k(\tau) = 0$, substitution of this ansatz into (2.20) and evaluation in $s = -\mathrm{i} + \delta_k$ and $s = \mathrm{i} + \delta_k$ yields

$$f_k(\mathrm{i} + \delta_k)\zeta_k^{(1)} + \frac{2\Gamma g k}{\Omega^2}\zeta_k^{(0)} = 0, \tag{2.29}$$

$$f_k(-\mathrm{i} + \delta_k)\zeta_k^{(0)} + \frac{2\Gamma g k}{\Omega^2}\zeta_k^{(1)} = 0. \tag{2.30}$$

These two equations admit non-trivial solutions if and only if

$$f_k(\mathrm{i} + \delta_k) f_k(-\mathrm{i} + \delta_k) - \left(\frac{2\Gamma g k}{\Omega^2}\right)^2 = 0. \tag{2.31}$$

2.2.1. *Faraday instability*

The special choice $\delta_k = 0$ in (2.31) yields the condition for the emergence of self-sustained Faraday waves at the subharmonic resonance. The dimensionless driving acceleration Γ_k necessary to make the wavenumber k unstable is then given by

$$\Gamma_k = \frac{\Omega^2 |f_k(\mathrm{i})|}{2gk} \tag{2.32}$$

https://doi.org/10.1017/jfm.2018.358 Published online by Cambridge University Press

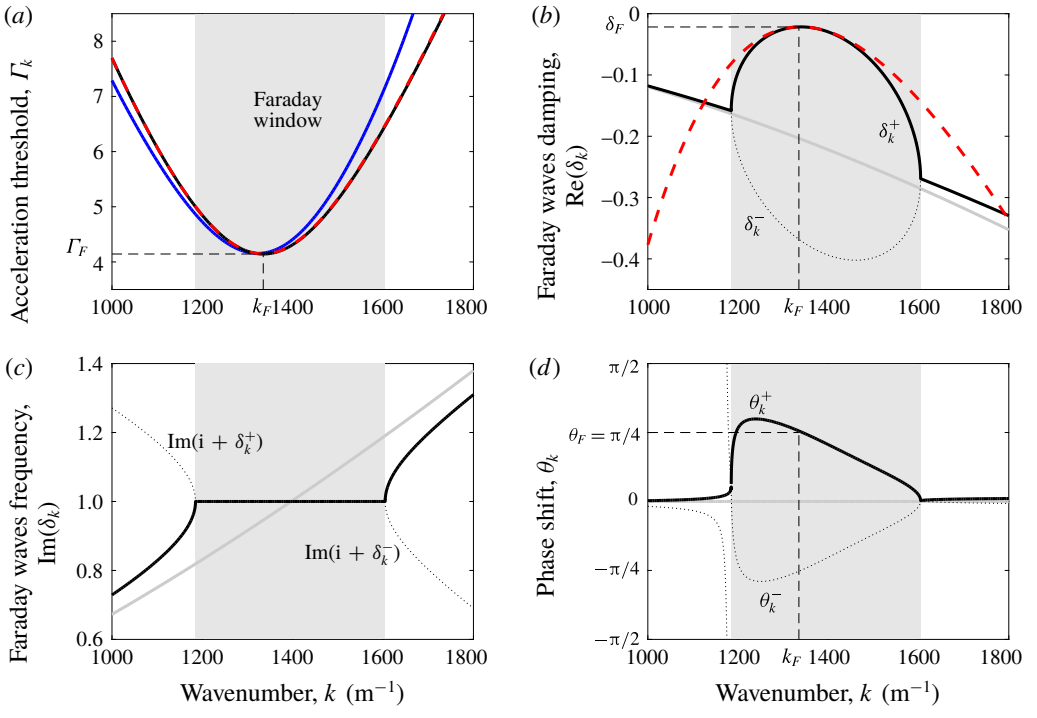


FIGURE 2. (Colour online) (*a*) Acceleration threshold Γ_k required to sustain waves of wavenumber k. The minimum of Γ_k gives the most unstable wavenumber, k_F. (*b*) Damping of the Faraday waves Re(δ_k). (*c*) Frequency of the Faraday wave Im(i + δ_k). (*d*) Phase shift θ_k of the Faraday waves with respect to the forcing signal. In (*a*), the blue curve represents the solution of the Floquet's ansatz with truncation to 4 harmonics (A 10), while the black curve corresponds to the truncation to 2 harmonics (2.32). In (*b*,*c*) the dotted line and the thick solid line represent equations (2.38) and (2.39), respectively. In (*d*), they represent (2.47). In (*a*,*b*) the red dashed curve is the low-viscosity approximation of the truncation to two harmonics (B 17) and (B 22). In (*b*,*c*) the damping and frequency of unforced waves ((2.24) and (2.25), respectively) are represented in light grey. In (*a*–*d*) all equations have been evaluated with numerical values of table 1. In particular, the distance to threshold $\mathcal{M} = (\Gamma_F - \Gamma)/\Gamma_F = 10$. The grey shade indicates the Faraday window, i.e. the range of wavenumbers k that produce waves locked to half the driving frequency.

since $f_k(s)$ is self-conjugated. This function Γ_k is represented in figure 2(*a*). There is always a global minimum of Γ_k that corresponds to the most unstable wavenumber, k_F:

$$\left.\frac{\partial \Gamma_k}{\partial k}\right|_{k_F} = 0. \tag{2.33}$$

The corresponding acceleration threshold is denoted $\Gamma_F = \Gamma_k(k_F)$. The effect of the truncation is seen in figure 2(*a*), where (2.32) is compared to the solution of the Floquet ansatz with a truncation to higher-order terms (appendix A). Close to the Faraday threshold k_F, the difference between the two truncations becomes negligible.

https://doi.org/10.1017/jfm.2018.358 Published online by Cambridge University Press

2.2.2. *Waves just below the Faraday threshold*

When the driving acceleration Γ is tuned slightly below the Faraday threshold Γ_F, some small complex detuning δ_k should arise for the wavenumbers $k \sim k_F$, as prescribed by (2.31). A good approximation of this detuning can be captured by expanding the function $f_k(\pm\mathrm{i} + \delta_k)$ to the second order in δ_k:

$$f_k(\pm\mathrm{i} + \delta_k) = f_k(\pm\mathrm{i}) + \delta_k \dot{f}_k(\pm\mathrm{i}) + \delta_k^2 \ddot{f}_k(\pm\mathrm{i})/2, \tag{2.34}$$

where $\dot{f}_k = \partial f_k/\partial s$. Substitution in (2.31) yields

$$\begin{aligned}&\frac{\delta_k^2}{2}(f_k(\mathrm{i})\ddot{f}_k(-\mathrm{i}) + f_k(-\mathrm{i})\ddot{f}_k(\mathrm{i}) + 2\dot{f}_k(\mathrm{i})\dot{f}_k(-\mathrm{i}))\\ &\quad + \delta_k(f_k(\mathrm{i})\dot{f}_k(-\mathrm{i}) + f_k(-\mathrm{i})\dot{f}_k(\mathrm{i})) + \left(\frac{2gk}{\Omega^2}\right)^2(\Gamma_k^2 - \Gamma^2) = 0.\end{aligned} \tag{2.35}$$

The coefficients of this second-order polynomial in δ_k are all real, because f_k and its derivatives are self-conjugated. If the corresponding discriminant is positive, i.e. if

$$\Gamma_k^2 - \Gamma^2 < \left(\frac{\Omega^2}{2gk}\right)^2 \frac{(f_k(\mathrm{i})\dot{f}_k(-\mathrm{i}) + f_k(-\mathrm{i})\dot{f}_k(\mathrm{i}))^2}{2(f_k(\mathrm{i})\ddot{f}_k(-\mathrm{i}) + f_k(-\mathrm{i})\ddot{f}_k(\mathrm{i}) + 2\dot{f}_k(\mathrm{i})\dot{f}_k(-\mathrm{i}))}, \tag{2.36}$$

then both solutions $\delta_k \in \mathrm{Re}$ and the resulting waves (cf. (2.28)) are locked at half the driving frequency, i.e. at $\Omega/2$ (figure 2*c*). For a given $\Gamma \lesssim \Gamma_F$, equation (2.36) is valid for a small range of k around k_F that we call the Faraday window (shaded regions in figure 2). Outside this range, waves are travelling waves with group velocity different from 0, and their frequency is detuned from the forcing frequency since the corresponding δ_k is complex. The latter waves compound the capillary wave packet by opposition to standing Faraday waves.

Equation (2.35) admits two solutions

$$\delta_k^{\pm} = -\frac{b}{2a}\left(1 \mp \sqrt{1 - \frac{4ac}{b^2}(\Gamma_k^2 - \Gamma^2)}\right), \tag{2.37}$$

where coefficients a, b and c are obtained by identification of (2.35) with $a\delta_k^2 + b\delta_k + c(\Gamma_k^2 - \Gamma^2) = 0$. Since $\Gamma_k \simeq \Gamma$ inside the Faraday window, these solutions can be expanded in Taylor series for $|4ac(\Gamma_k^2 - \Gamma^2)/b^2| \ll 1$. To the first order,

$$\delta_k^- = -\frac{b}{a}\left[1 + O\left(\frac{ac(\Gamma_k^2 - \Gamma^2)}{b^2}\right)\right] \simeq -\frac{2(f_k(\mathrm{i})\dot{f}_k(-\mathrm{i}) + f_k(-\mathrm{i})\dot{f}_k(\mathrm{i}))}{f_k(\mathrm{i})\ddot{f}_k(-\mathrm{i}) + f_k(-\mathrm{i})\ddot{f}_k(\mathrm{i}) + 2\dot{f}_k(\mathrm{i})\dot{f}_k(-\mathrm{i})}, \tag{2.38}$$

and

$$\delta_k^+ = -\frac{c(\Gamma_k^2 - \Gamma^2)}{b}\left[1 + O\left(\frac{ac(\Gamma_k^2 - \Gamma^2)}{b^2}\right)\right] \simeq -\frac{(2gk/\Omega^2)^2(\Gamma_k^2 - \Gamma^2)}{f_k(\mathrm{i})\dot{f}_k(-\mathrm{i}) + f_k(-\mathrm{i})\dot{f}_k(\mathrm{i})}. \tag{2.39}$$

The real and imaginary parts of these solutions $\delta_k^{\pm}$ are represented in figures 2(*b*) and 2(*c*), respectively. The imaginary part $\mathrm{Im}(\delta_k^{\pm})$ corresponds to some detuning from the Faraday frequency $\Omega/2$, and it is identically 0 in the Faraday window around k_F. The corresponding waves are standing. Outside from this Faraday window, $\mathrm{Im}(\delta_k^{\pm} + \mathrm{i})$

https://doi.org/10.1017/jfm.2018.358 Published online by Cambridge University Press

increases with k, so the group velocity is positive and the solution corresponds to travelling waves. Inside the Faraday window, the real part of δ_k^- remains largely negative so it describes Faraday waves that are strongly damped and that vanish quickly. By contrast, when Γ approaches Γ_F, the real part of δ_k^+ can be arbitrarily close to 0 for $k \simeq k_F$, in the Faraday window. Consequently, δ_k^+ describes some long-lived standing Faraday waves. These latter waves are those observed to travel with the walker, and they are crucial to the description of its dynamics since their amplitude remains significant during many rebounds.

The memory Me of the waves, initially described by Eddi *et al.* (2011), is defined as the damping time of these long-lived Faraday waves, expressed in the number of rebounds of the droplet. Since the bouncing period corresponds to the Faraday period $T_F = 4\pi/\Omega$, the memory is given by

$$Me = \frac{-1}{2\pi\delta_F} \simeq \frac{1}{4\pi} \frac{f_F(\mathrm{i})\dot{f}_F(-\mathrm{i}) + f_F(-\mathrm{i})\dot{f}_F(\mathrm{i})}{|f_F(\mathrm{i})|^2} \mathcal{M}, \tag{2.40}$$

where $\delta_F = \lim_{k\to k_F} \mathrm{Re}(\delta_k^+)$ and where

$$\mathcal{M} = \frac{\Gamma_F}{\Gamma_F - \Gamma} \tag{2.41}$$

is called the 'distance to the Faraday threshold'. This latter parameter has often been used as a proxy for the memory in experimental studies of walkers (Eddi *et al.* 2011).

The expression of δ_k^+ in (2.39) may be particularised to the wavenumbers around k_F, which will likely compose the major part of the walker's wave field. For $\Gamma \lesssim \Gamma_F$ (i.e. for $\mathcal{M} \gg 1$), we can expand δ_k^+ in a Taylor series around k_F. Recalling that $\partial\Gamma_k/\partial k = 0$ in $k = k_F$, we obtain

$$\begin{aligned}\delta_k^+ \;=\; & -\left[\frac{\Gamma_F(2gk_F/\Omega^2)^2}{(f_F(\mathrm{i})\dot{f}_F(-\mathrm{i}) + f_F(-\mathrm{i})\dot{f}_F(\mathrm{i}))}\left(\frac{\partial^2\Gamma_k}{\partial k^2}\right)_F (k-k_F)^2 + O((k-k_F)^3)\right] \\ & - \frac{2}{\mathcal{M}}\left[\frac{\Gamma_F^2(2gk_F/\Omega^2)^2}{f_F(\mathrm{i})\dot{f}_F(-\mathrm{i}) + f_F(-\mathrm{i})\dot{f}_F(\mathrm{i})} + O(k-k_F)\right] + O(\mathcal{M}^{-2}),\end{aligned} \tag{2.42}$$

where $f_F = f_{k_F}$ and $\dot{f}_F = \dot{f}_{k_F}$. This approximation of δ_k^+ is plotted with a red dashed line in figure 2(*b*). We identify this expression with $\delta_k^+ = \delta_F - D(k-k_F)^2 + O((k-k_F)^3) + O(\mathcal{M}^{-1})$ and define the diffusion coefficient D as

$$D = -\frac{1}{2}\frac{\partial^2\delta_k^+}{\partial k^2}\bigg|_{k=k_F} = \frac{\Gamma_F(2gk_F/\Omega^2)^2}{(f_F(\mathrm{i})\dot{f}_F(-\mathrm{i}) + f_F(-\mathrm{i})\dot{f}_F(\mathrm{i}))}\left(\frac{\partial^2\Gamma_k}{\partial k^2}\right)_F. \tag{2.43}$$

Since

$$\left(\frac{\partial^2\Gamma_k}{\partial k^2}\right)_F = \frac{1}{2k_F^2\Gamma_F}\frac{\partial^2(k\Gamma_k)^2}{\partial k^2}\bigg|_F - \frac{\Gamma_F}{k_F^2} \tag{2.44}$$

and $k^2\Gamma_k^2 = \Omega^4|f_k(\mathrm{i})|^2/(2g)^2$, D can be expressed in terms of f_k as

$$D = \frac{(\partial^2|f_k(\mathrm{i})|^2/\partial k^2)_F - 2|f_F(\mathrm{i})|^2/k_F^2}{2(f_F(\mathrm{i})\dot{f}_F(-\mathrm{i}) + f_F(-\mathrm{i})\dot{f}_F(\mathrm{i}))}. \tag{2.45}$$

https://doi.org/10.1017/jfm.2018.358 Published online by Cambridge University Press

The amplitude ζ_k^+ of the long-lived Faraday waves (respectively ζ_k^- for short-lived waves) is given from (2.29):

$$\zeta_k^{\pm}(\tau) \propto \mathrm{e}^{\delta_k^{\pm}\tau}\left(\mathrm{e}^{\mathrm{i}\tau} - \frac{f_k(\mathrm{i}+\delta_k^{\pm})}{2\Gamma gk/\Omega^2}\mathrm{e}^{-\mathrm{i}\tau}\right). \tag{2.46}$$

We introduce

$$\theta_k^{\pm} = \arctan\left(\frac{\mathrm{Im}\{f_k(\mathrm{i}+\delta_k^{\pm})\}}{2\Gamma gk/\Omega^2 - \mathrm{Re}\{f_k(\mathrm{i}+\delta_k^{\pm})\}}\right), \tag{2.47}$$

in order to express the total wave field $\zeta_k(\tau)$ as

$$\zeta_k(\tau) = A_k^+\mathrm{e}^{\delta_k^+\tau}\cos(\tau+\theta_k^+) + A_k^-\mathrm{e}^{\delta_k^-\tau}\cos(\tau+\theta_k^-), \tag{2.48}$$

where A_k^+ and A_k^- stand for the relative amplitude of long-lived and short-lived waves, respectively. The angles $\theta_k^{\pm}$ then correspond to the phase shift between these waves and the driving acceleration. They are represented in figure 2(*d*). Outside the Faraday window, they are both close to 0, while inside the Faraday window they strongly vary with k in a non-trivial way. Remarkably around k_F, these phase shifts are $\theta_F^{\pm} \simeq \pm\pi/4$.

2.3. *Single impact of a droplet*

We now consider the impact of a droplet at the surface of the liquid at a time τ_i. While sophisticated theoretical frameworks have been developed in order to accurately calculate the interaction of a droplet with the surface of a liquid (Moláček & Bush 2012; Molacek & Bush 2013; Milewski *et al.* 2015), we shall, for illustration purposes, employ a rather simplified description of the droplet impact. Namely, we model its temporal profile with a delta function. The corresponding dimensionless pressure exerted by the droplet on the liquid bath is then

$$\Pi_k(\tau) = \delta(\tau-\tau_i)v_k. \tag{2.49}$$

By integrating (2.22) across the delta kick, it is shown that v_k corresponds to the negative change of velocity of ζ_k following impact. If the surface is perfectly flat and at rest before the impact, the wave profile is axisymmetric, i.e. $\zeta_k(\tau) = \zeta_k(\tau)$. The initial conditions in $\tau \to \tau_i^+$ are $\zeta_k = 0$ and $\partial\zeta_k/\partial\tau = -v_k$. They determine the coefficients $A_k^{\pm}$ of (2.48):

$$A_k^{\pm} = -\frac{2\cos(\tau_i+\theta_k^{\mp})v_k\mathrm{e}^{-\delta_k^{\pm}\tau_i}}{(\delta_k^{\pm}-\delta_k^{\mp})(\cos(2\tau_i+\theta_k^{\pm}+\theta_k^{\mp})+\cos(\theta_k^{\pm}-\theta_k^{\mp})) - 2\sin(\theta_k^{\pm}-\theta_k^{\mp})}. \tag{2.50}$$

Transforming back to the spatial domain according to (2.9) then yields the radially symmetric surface wave profile

$$\zeta_1(r,\tau) = \int_0^{\infty}\zeta_k(\tau)\mathrm{J}_0(kr)k\,\mathrm{d}k \tag{2.51}$$

that is generated by a delta kick, where J_0 is the Bessel function of the first kind of order zero.

https://doi.org/10.1017/jfm.2018.358 Published online by Cambridge University Press

At large times $\tau \gg \tau_i$ for $\Gamma \lesssim \Gamma_F$, the wave field is dominated by the contribution ζ_k^+, so

$$\zeta_1(r,\tau) = \int_0^\infty B_k^+(\tau_i)\cos(\tau+\theta_k^+)\mathrm{e}^{\delta_k^+(\tau-\tau_i)}\mathrm{J}_0(kr)k\,\mathrm{d}k, \tag{2.52}$$

where $B_k^+(\tau_i) = A_k^+\mathrm{e}^{\delta_k^+\tau_i}$. With the expansion $\delta_k^+ = \delta_F - D(k-k_F)^2 + O((k-k_F)^3) + O(\mathcal{M}^{-1})$, we can then approximate this integral thanks to the saddle-point method in the formal limit $\tau\to\infty$. Calculations detailed in appendix C yield:

$$\zeta_1(r,\tau) \simeq B_F^+(\tau_i)k_F\sqrt{\frac{\pi}{D(\tau-\tau_i)}}\cos(\tau+\theta_F^+)\mathrm{J}_0(k_Fr)\exp\left[-\frac{\tau-\tau_i}{2\pi Me}-\frac{r^2}{4D(\tau-\tau_i)}\right], \tag{2.53}$$

which is at least valid when $k_Fr \ll 1$ and $k_Fr \gg 1$. Equation (2.53) is the impulse response of the Faraday waves in the long-time limit. According to Duhamel's principle, the response to any sophisticated impact signal $\Pi_k(\tau)$ can be inferred by convoluting this impulse response with $\Pi_k(\tau)$.

Equation (2.53) may be compared to the main previous model of waves generated by a single impact of a droplet (1.5), which can be rewritten as:

$$\zeta(r,t) = \frac{A(\tau_i)}{\sqrt{\tau-\tau_i}}\cos(\tau)\mathrm{J}_0(k_Fr)\exp\left(-\frac{\tau-\tau_i}{2\pi Me}\right). \tag{2.54}$$

The main additions of (2.53) to (2.54) are (i) the phase shift θ_F^+, (ii) a diffusive spreading in the exponential decay (diffusion coefficient D) and (iii) a well-defined amplitude B_F^+ that depends on the impact phase τ_i through (2.50). Modifications similar to (ii) and (iii) can be deduced with additional calculations, starting from the theory of Moláček & Bush (2013).

2.4. *Surface waves emitted by a walker*

The long-lived Faraday wave generated by a walker is obtained by superimposing impulse responses corresponding to each droplet impact at time τ_n and position $\boldsymbol{r}_n$. In the absence of other walkers, submerged boundaries or body forces, a walker bounces periodically every Faraday period and moves in a straight line at constant speed V_w. Consequently,

$$\tau_n = \tau_i + 2\pi n, \quad n\in\mathbb{Z}, \quad \text{and} \quad \boldsymbol{r}_n = -(\tau-\tau_n)\boldsymbol{v}, \tag{2.55a,b}$$

where $v = 2V_w/\Omega$ is the normalised walking speed. The origin $\boldsymbol{r}=0$ is set where the walker is at time τ. The Faraday wave field is then given by

$$\zeta_w(\boldsymbol{r},\tau) = \sum_{n=-\infty}^{[(\tau-\tau_i)/2\pi]}\zeta_1(|\boldsymbol{r}-\boldsymbol{r}_n|,\tau-2\pi n), \tag{2.56}$$

where $[(\tau-\tau_i)/2\pi]$ denotes the largest integer smaller than $(\tau-\tau_i)/2\pi$.

This sum is evaluated in appendix D. It yields

$$\begin{aligned}\zeta_w(\boldsymbol{r},\tau) \;=\; & \frac{B_F^+k_F}{2\sqrt{D}}\cos(\tau+\theta_F^+)\exp\left(-\frac{vr\cos\theta}{2D}\right)\\ & \times\int_{-\pi}^{\pi}\mathrm{d}\varphi\frac{\exp[\mathrm{i}k_Fr\sin(\theta-\varphi)]}{\sqrt{a-\mathrm{i}k_Fv\sin\varphi}}\exp\left(-\frac{r}{\sqrt{D}}\sqrt{a-\mathrm{i}k_Fv\sin\varphi}\right),\end{aligned} \tag{2.57}$$

https://doi.org/10.1017/jfm.2018.358 Published online by Cambridge University Press

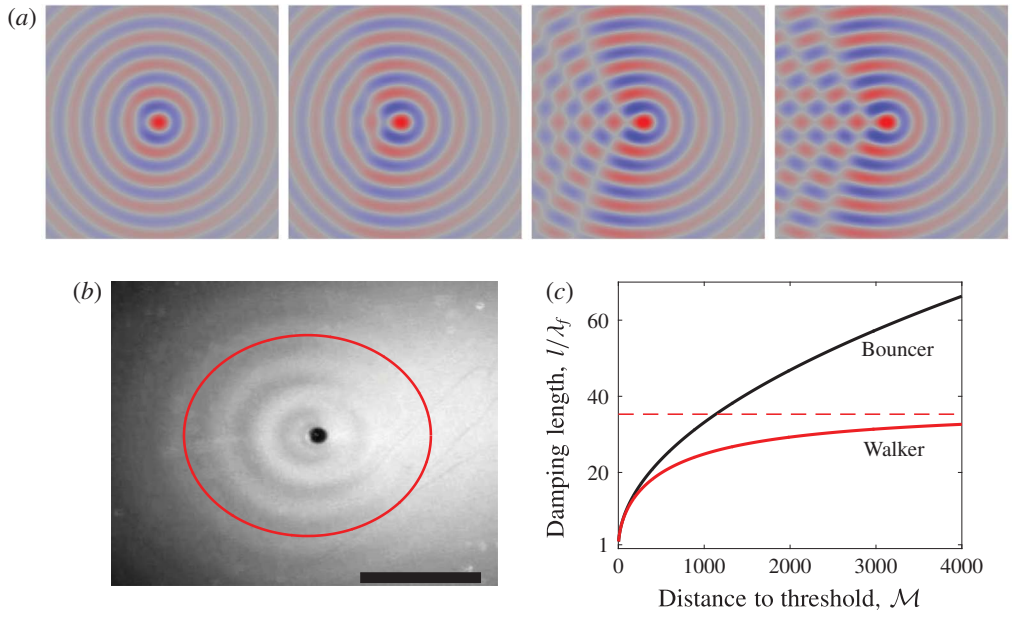


FIGURE 3. (Colour online) (*a*) Asymmetric wave field of a walker, calculated numerically from equation (2.57), for different values of the memory Me. From left to right, $Me = 7.7$, $Me = 16$, $Me = 82$ and $Me = 447$ respectively. The walker velocity is fixed to $V_w = 10$ mm s^{-1} from left to right, and other parameters are given in table 1. The field of view is 4×4 cm. (*b*) Anisotropic damping length $l(\theta)$, compared to the experimental wave field of a walker. The red curve corresponds to (2.60) with $\mathcal{M} = 10$ and other numerical values from table 1. In the experiment, the walking speed is 10 mm s^{-1} and $\mathcal{M} = 10$. The scale bar is 1 cm. (*c*) Lateral damping length ($\theta = \pi/2$) for a bouncer (black curve, $V_w = 0$) and a walker (red curve, $V_w = 11$ mm s^{-1}), as a function of the distance to threshold $\mathcal{M}$.

where $\cos\theta = \boldsymbol{v}\cdot\boldsymbol{r}/(vr)$ and

$$a = \frac{1}{2\pi Me} + \frac{v^2}{4D}. \tag{2.58}$$

The corresponding wave field can be calculated by numerically integrating (2.57). Some characteristic wave fields are shown in figure 3(*a*), for different values of the memory Me. With increasing Me, the sum includes significant contributions from an increasing number of past impacts. Some interferences appear in the wake of the walker, similarly to what is seen experimentally (Eddi *et al.* 2011).

In the limit of small walking speed and low memory ($2\pi Mek_F v \ll 1$), the integral (2.57) can be solved analytically (appendix D):

$$\zeta_w(\boldsymbol{r},\tau) = \frac{B_F^+ k_F}{\sqrt{v^2 + \dfrac{2D}{\pi Me}}} \cos(\tau + \theta_F^+) \mathrm{J}_0\left(k_F \left| \boldsymbol{r} + \frac{r}{\sqrt{v^2 + \dfrac{2D}{\pi Me}}}\boldsymbol{v} \right|\right) \exp[-r/l(\theta)], \tag{2.59}$$

https://doi.org/10.1017/jfm.2018.358 Published online by Cambridge University Press

where

$$l(\theta) = \frac{2D}{v\cos\theta + \sqrt{v^2 + \dfrac{2D}{\pi Me}}}. \tag{2.60}$$

Equation (2.59) corresponds to a Doppler-shifted Bessel profile which is exponentially attenuated on an length scale $l(\theta)$ that varies with direction θ. The resulting wavelength is smaller in front of the walker and larger in its wake. The damping distance is smaller in front of the walker than in its wake, as illustrated in figure 3(*b*).

For either larger walking speed of larger memory, interferences between Bessel functions are more complex and solving the integral (2.57) is not straightforward. Nevertheless, an upper bound to the wave field can be found, as derived in appendix D:

$$\left|\frac{\zeta_w(\boldsymbol{r},\tau)}{\cos(\tau+\theta_F^+)}\right| \leqslant \frac{\pi B_F^+ k_F}{\sqrt{Da}}\exp\left[-\frac{r}{l(\theta)}\right]. \tag{2.61}$$

This bound indicates that the Faraday waves emitted by the walkers are always subjected to the same exponential spatial damping $l(\theta)$ defined in (2.60).

In the case of a bouncer ($v = 0$), this damping length $l(\theta) = \sqrt{2\pi DMe}$ is independent of θ (axisymmetric damping) and it grows indefinitely with increasing memory. At the Faraday threshold (infinite memory), a bouncer would generate waves that are not spatially damped. By contrast, waves are always spatially damped for a walker with finite speed v. Indeed, when $Me \to \infty$, $l(\theta) \to 2D/[v(1+\cos\theta)]$. This horizontal asymptote is illustrated in figure 3(*c*). Hence, equation (2.61) predicts a finite spatial damping even at infinite memory, and this for all directions except $\theta = \pi$.

2.5. *Approximations specific to the experimental regime of walkers*

The subthreshold Faraday wave theory developed in previous sections is now particularised to the regime of walkers that corresponds to most experiments reported up to now (Bush 2015). Typical values for each parameter are summarised in table 1. The liquid is silicone oil with density $\rho = 956$ kg m^{-3}, surface tension $\sigma = 20.6 \times 10^{-3}$ N m^{-1} and viscosity $\nu = 20 \times 10^{-6}$ m^2 s^{-1}. The bath is vibrated sinusoidally at a frequency $\Omega/2\pi = 80$ Hz.

In the limit of vanishing viscosity ν, $\gamma_k \to 0$, and $f_k(i) \to \omega_k^2 - 1$. Therefore, according to (2.32), the instability threshold $\Gamma_F \to 0$ in $k = k_0$ such that $\omega_0^2 = \omega_{k_0}^2 = 1$. For a walker, $k_0 = 1319.5$ m^{-1}, which corresponds to a wavelength of 4.76 mm, already close to experimental observations (Eddi *et al.* 2011). The corresponding damping (at $\nu = 20$ cS) is $\gamma_0 = \gamma_{k_0} = 0.277$. Although this value is not much smaller than 1, we can perform a Taylor expansion in γ_0 for each quantity of interest.

First, we prove in appendix B that the most unstable wavenumber k_F, defined from (2.33), can be approximated by:

$$k_F = k_0 + \frac{1}{2c_0}\gamma_0^{3/2} - \frac{2+k_0c_0}{2k_0c_0^2}\gamma_0^2 + \frac{12+k_0c_0}{8k_0c_0^2}\gamma_0^{5/2} + \left(\frac{1}{4k_0c_0^2} - \frac{d_0}{8c_0^3}\right)\gamma_0^3 + O(\gamma_0^{7/2}), \tag{2.62}$$

https://doi.org/10.1017/jfm.2018.358 Published online by Cambridge University Press

where $d_0 = (\partial^2\omega_k^2/\partial k^2)(k_0) = 24\sigma k_0/\rho\Omega^2$ and $c_0 = (\partial\omega_k/\partial k)(k_0) = (2(g + 3\sigma k_0^2/rho)/\Omega^2)$ is the group velocity of free waves around the wavenumber k_0. For walkers, $c_0 = 0.97$ mm (which corresponds to a speed $\Omega c_0/2 = 0.24$ m s^{-1}) and the approximation (2.62) gives $k_F \simeq 1338.7$ m^{-1} and $\lambda_f = 4.693$ mm, while a numerical computation of the exact solution of (2.33) without any approximation except the Floquet's first-order truncation would give $k_F = 1334.8$ m^{-1} and $\lambda_f = 4.707$ mm.

From appendix B, it follows that

$$\left.\begin{aligned} \omega_F^2 &= 1 + \gamma_0^{3/2} - \frac{2 + k_0c_0}{k_0c_0}\gamma_0^2 + \frac{12 + k_0c_0}{4k_0c_0}\gamma_0^{5/2} + O(\gamma_0^3), \\ \gamma_F &= \gamma_0 + \frac{\gamma_0^{5/2}}{k_0c_0} + O(\gamma_0^3). \end{aligned}\right\} \tag{2.63}$$

Equation (2.32) for the corresponding instability threshold $\Gamma_F = \Gamma_k(k_F)$ is then approximated by:

$$\Gamma_F = \frac{\Omega^2}{gk_0}\gamma_0 - \frac{\Omega^2}{2gk_0}\gamma_0^{3/2} + O(\gamma_0^{5/2}). \tag{2.64}$$

The first term of Γ_F corresponds to the threshold predicted from the damped Matthieu equation (1.3) with a phenomenological factor $\alpha = 2$ (Sampara & Gilet 2016). Since for walkers $\gamma_0 = 0.277$, a limitation to this first term would yield $\Gamma_F = 5.41$. Considering instead the first two terms yields $\Gamma_F = 3.985$. The exact solution of (2.32) obtained numerically is $\Gamma_F = 4.144$, which is very close to experimental values. The correction in $\gamma_0^{3/2}$ is therefore a considerable improvement of this theory with respect to the damped Matthieu equation.

The memory Me defined in (2.40) can be approximated by:

$$Me = \frac{\mathcal{M}}{2\pi\gamma_0}\left(1 + \frac{\gamma_0^{1/2}}{2} + \frac{\gamma_0}{4} + O(\gamma_0^{3/2})\right). \tag{2.65}$$

It is therefore inversely proportional to the viscosity ν and an inviscid fluid would yield a theoretically infinite memory. In the case of walkers, $(1 + \gamma_0^{1/2}/2 + \gamma_0/4)/2\pi\gamma_0 \sim 0.76$, which is fairly close to unity. In previous work on walkers, Me has often been mixed up with the distance to threshold $\mathcal{M}$, without much consequence. Close to threshold ($\Gamma \lesssim \Gamma_F$), the damping factor of short-lived Faraday waves $\delta_F^- = -2\gamma_0 + O(\gamma_0^{3/2})$ is significantly more negative than the damping of long-lived waves $\delta_F^+ = -1/(2\pi Me)$.

The diffusion coefficient D associated with long-lived Faraday waves and defined in (2.45) is approximated by

$$D = \frac{c_0^2}{2\gamma_0}\left(1 + \frac{\gamma_0^{1/2}}{2} + O(\gamma_0)\right) \tag{2.66}$$

which is about $D \simeq 4.40$ mm^2 for a walker.

The phase shift of long-lived and short-lived Faraday waves near the Faraday threshold is:

$$\theta_F^{\pm} = \pm\pi/4 + O(\gamma_0), \tag{2.67}$$

https://doi.org/10.1017/jfm.2018.358 Published online by Cambridge University Press

and consequently,

$$A_F^{\pm} = v_F \cos\left(\tau_i \mp \frac{\pi}{4}\right) \mathrm{e}^{-\delta_F^{\pm}\tau_i} + O(\gamma_0) \quad \text{and} \quad B_F^{+} = v_F \cos\left(\tau_i - \frac{\pi}{4}\right) + O(\gamma_0). \quad (2.68a,b)$$

The long-lived impulse response (2.53) then becomes:

$$\zeta_1(r,\tau) \simeq v_F k_F \sqrt{\frac{\pi}{D(\tau-\tau_i)}} \mathrm{J}_0(k_F r) \cos\left(\tau_i - \frac{\pi}{4}\right) \cos\left(\tau + \frac{\pi}{4}\right) \times \exp\left[-\frac{\tau-\tau_i}{2\pi M e} - \frac{r^2}{4D(\tau-\tau_i)}\right], \quad (2.69)$$

which reads in dimensional form,

$$\zeta_1(r,t) \simeq v_F k_F \sqrt{\frac{2\pi}{D\Omega(t-t_i)}} \mathrm{J}_0(k_F r) \cos\left(\frac{\Omega t_i}{2} - \frac{\pi}{4}\right) \cos\left(\frac{\Omega t}{2} + \frac{\pi}{4}\right) \times \exp\left[-\frac{(t-t_i)}{MeT_F} - \frac{r^2}{2D\Omega(t-t_i)}\right]. \quad (2.70)$$

The upper bound (2.61) on the wave field of a walker that moves at constant normalised speed v becomes

$$\left|\frac{\zeta_w(\boldsymbol{r},\tau)}{\cos(\tau+\pi/4)}\right| \leqslant \frac{2\pi v_F k_F \cos(\tau_i - \pi/4)}{\sqrt{v^2 + \dfrac{c_0^2}{\mathcal{M}}}} \exp\left[-\frac{r}{l(\theta)}\right] \quad (2.71)$$

with

$$l(\theta) \simeq \frac{c_0^2}{2\gamma_0[v\cos\theta + \sqrt{v^2 + c_0^2/\mathcal{M}}]}. \quad (2.72)$$

For distance to threshold $\mathcal{M} \gg c_0^2/v^2$ (which is approximately 490 for walkers),

$$l(0) \simeq \frac{c_0^2}{4\gamma_0 v} \simeq 1.9 \text{ cm}, \quad \text{and} \quad l(\pi) \simeq \frac{\mathcal{M}}{\gamma_0}. \quad (2.73a,b)$$

The damping length l can therefore be as large as wanted in the wake of the walker ($\theta = \pi$), but it is strongly limited in front of the walker, independently of $\mathcal{M}$. Nevertheless, $l(0)$ could be increased by decreasing γ_0, i.e. by decreasing viscosity and associated dissipation.

At sufficiently low $\mathcal{M}$, given by (2.59) is approximated by:

$$\zeta_w(\boldsymbol{r},t) \simeq \frac{v_F k_F}{\sqrt{v^2 + \dfrac{c_0^2}{\mathcal{M}}}} \cos\left(\tau_i - \frac{\pi}{4}\right) \cos\left(\tau + \frac{\pi}{4}\right) \mathrm{J}_0\left[k_F \left|\boldsymbol{r} + \frac{r}{\sqrt{v^2 + \dfrac{c_0^2}{\mathcal{M}}}}\boldsymbol{v}\right|\right] \mathrm{e}^{-r/l(\theta)}. \quad (2.74)$$

https://doi.org/10.1017/jfm.2018.358 Published online by Cambridge University Press

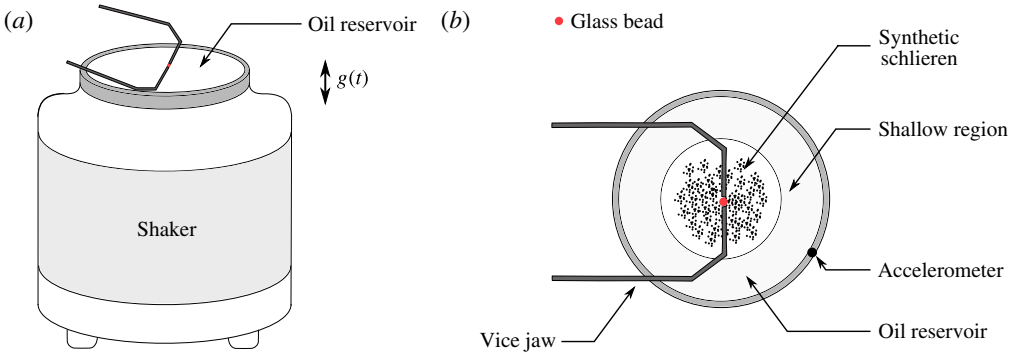


FIGURE 4. (Colour online) Tilted view (*a*) and top view (*b*) of the experimental set-up. A large transparent reservoir of oil is mounted on top of a shaker. Below the reservoir a transparent sheet is printed with a synthetic schlieren. The border of the reservoir is a shallow region where surface waves are strongly damped. A glass bead is released on demand above the reservoir with a vice jaw opened with a translation stage. The acceleration of the reservoir is measured with an accelerometer placed on the border of the reservoir.

This approximation is only valid when $k_F v/a \ll 1$ (appendix D), which here reduces to

$$\mathcal{M} \ll \left(\frac{k_F v}{\gamma_0} - \frac{v^2}{c_0^2}\right)^{-1}. \tag{2.75}$$

This limit is $\mathcal{M} \ll 4.9$ for a walker at speed $V_w = 11$ mm s^{-1}. Furthermore, since $\mathcal{M} \ll c_0^2/v^2 \simeq 490$, the Doppler shift along the walker trajectory in (2.74) can be approximated by

$$k_{Doppler} = k_F \pm \frac{v}{c_0}\sqrt{\mathcal{M}}. \tag{2.76}$$

This expression is very similar to the one obtained numerically in Milewski *et al.* (2015).

3. Experimental observation of the surface waves emitted by a localised impact

This section aims at validating experimentally the theory of subthreshold surface waves developed in § 2. Specifically, we characterise (i) the spatial damping of the Faraday waves upon a single impact, (ii) the phase shift between these waves and the shaker position and (iii) the dependence of the wave amplitude on the phase of impact. These three points are major additions of the present theory with respect to previous models of the Faraday waves generated by walkers (Eddi *et al.* 2011; Moláček & Bush 2013).

3.1. *Experimental set-up*

The goal of the experiment is to finely quantify the spatio-temporal evolution of the surface waves generated by the single localised impact of a bead. The experimental set-up, depicted in figure 4, comprises a transparent cylindrical reservoir of diameter

https://doi.org/10.1017/jfm.2018.358 Published online by Cambridge University Press

22 cm filled with approximately 5 mm of silicone oil (Sigma-Aldrich). The reservoir is delimited by a shallow region (width 3 cm, depth <1 mm), thanks to which surface waves are strongly damped. This trick allows us to eliminate the additional waves generated by the meniscus at the boundaries of the reservoir (Bechhoefer *et al.* 1995; Nguyem Thu Lam & Caps 2011). The reservoir is also large enough (22 cm $\simeq 46\lambda_f$) to avoid confinement effects that may stabilise the bath when the bath diameter is less than 10 λ_f (Nguyem Thu Lam & Caps 2011). The reservoir is placed on top of an electromagnetic shaker (V400LT, Data Physics). The shaker motion is accurately controlled via an accelerometer tightly fixed on the reservoir, a computer interface and a feedback loop, as detailed in Sampara & Gilet (2016). The resulting effective gravity acceleration is $g(t) = g(1 + \Gamma \cos \Omega t)$. The frequency is fixed to $\Omega = 2\pi 80$ s^{-1}.

The bead is made of glass and its diameter is 1 mm. A device that can release the bead on demand is placed at 1 cm above the bath. It consists in a vice with two jaws that grip the bead. It is mechanically insulated from the shaker, so it is not sensitive to its vibrations. A translation stage allows us to open the vice and release the bead. The bead does not acquire any significant velocity from the vice, so it starts falling from rest.

Measurements must be gathered over many Faraday periods, with a time resolution well below the shaker period $2\pi/\Omega$. Therefore, we here use high-speed imaging (Phantom MIRO110), with an acquisition frequency of 4000 fps (i.e. 50 frames per period of the shaker). The shaker is illuminated with 4 home-made high-power LEDs to ensure strong illumination of the waves while limiting the associated heating. Thanks to a semi-refringent mirror placed at 45° above the shaker, optical paths of both illumination and recording are vertical near the bath surface. Thanks to a macro lens Zeiss Milvus 2/100M, the spatial resolution is brought down to 70 µm by pixel. The camera is synchronised with the shaker thanks to a DACQ (National Instruments) and a Labview interface that returns the impact phase τ_i, with respect to the Faraday period T_F. Details on this crucial synchronisation are provided in appendix E.

The free-surface synthetic schlieren technique developed by Moisy, Rabaud & Salsac (2009) is well adapted to measure wave elevations in real time. It consists in placing a transparent sheet printed with randomly spaced dots (dot diameter 100 µm, 50 % density) over a white background at the bottom of the reservoir. The image of these dots moves owing to the light refraction at the free surface. The displacement of the imaged dots is therefore related to the local slope of the free surface. This technique was already successfully applied to measure the 3-D shape of the long-lived Faraday waves generated by walkers, with an acquisition frequency lower than $\Omega/(2\pi)$ (Eddi *et al.* 2011; Damiano *et al.* 2016). However, in its original form, it is not well suited to the measurements intended here. Indeed, it requires a large field of view that must not be obstructed by the device which would drop the bead. Moreover, owing to the limited amount of information (3 GB) that can be acquired by a high-speed camera in a single shot, the recording duration at full spatial resolution would be a fraction of a second, which is definitely not sufficient to capture the long-term behaviour of Faraday waves. Finally, the reconstruction algorithm of Moisy's technique would demand large computational resources. In order to circumvent these limitations, we here use an adaptation of Moisy's technique. Since the wave field is known to be axisymmetric, we restrict the field of view to a radial zone of 2×15 mm from the impact point. This allows us to record much longer films (several seconds at 4000 fps), without any obstruction of the field of view by the bead-releasing device. The displacement of the imaged dots is calculated along a radius from impact point. The one-dimensional radial gradient

https://doi.org/10.1017/jfm.2018.358 Published online by Cambridge University Press

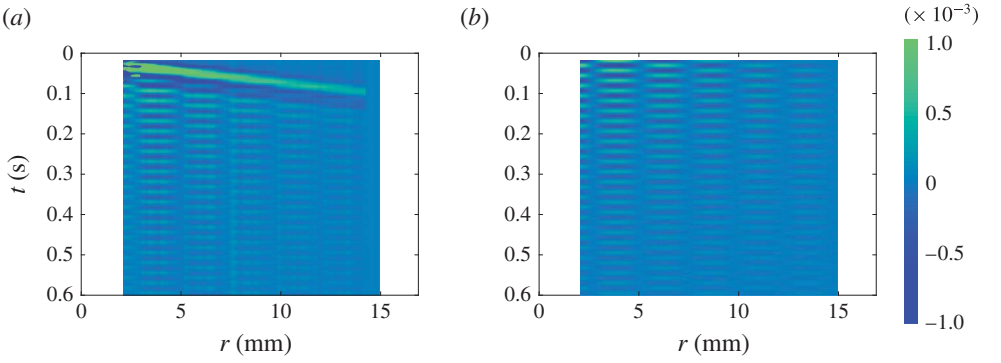


FIGURE 5. (Colour online) Qualitative comparison of the spatio-temporal evolution of the dimensionless radial wave gradient $\partial_r\zeta(r,\,t)$, represented here with a colour code. The impact is located in $(r,\,t)=(0,\,0)$. (*a*) Experiment at $\mathcal{M}=30$ and $\nu=20$ cS. Experimental parameters are gathered in table 1. (*b*) Theoretical prediction (3.1).

of the elevation $\zeta(r,\,t)$ is then calculated with a 1-D adaptation of the reconstruction algorithm detailed in Moisy *et al.* (2009). The restriction to a quasi-1-D wave pattern severely decreases the computational time of the reconstruction. However, it can be shown that the 1-D algorithm does not benefit anymore from the error compensation mechanism present in the 2-D algorithm. In order to limit the measurement error, we first remove most of the noise with deshaking and median filters. We also avoid the error build-up inherent to the spatial integration of $\partial_r\zeta$ to obtain $\zeta(r,\,t)$. We instead directly compare the measured $\partial_r\zeta$ to the theoretical prediction

$$\frac{\partial\zeta_1}{\partial r}(r,\,t) \;=\; -v_F k_F\sqrt{\frac{2\pi}{D\Omega(t-t_i)}}\cos\left(\frac{\Omega t_i}{2}-\frac{\pi}{4}\right)\cos\left(\frac{\Omega t}{2}+\frac{\pi}{4}\right)$$
$$\times\left[\mathrm{J}_1(k_F r)+\frac{r\mathrm{J}_0(k_F r)}{D\Omega(t-t_i)}\right]\exp\left[-\frac{(t-t_i)}{MeT_F}-\frac{r^2}{2D\Omega(t-t_i)}\right]. \qquad (3.1)$$

Several input parameters are systematically varied, including the impact phase of the bead relative to the shaker, the shaker amplitude and corresponding distance to threshold $\mathcal{M}$, and the liquid viscosity (5 cS and 20 cS silicone oil).

3.2. *Spatio-temporal evolution of the wave field*

A typical evolution of the wave field is represented in the space–time diagram of figure 5(*a*). We observe that the impact first generates a large capillary wave packet that travels radially outwards with an almost constant velocity of 16 cm s^{-1}. The long-lived Faraday waves described in § 2 are observed in the wake of this wave packet. They have a pulsation $\Omega/2$ and a wavelength $2\pi/k_F\simeq 4.7$ mm. The surface appears still in the region that is not yet visited by the wave packet (i.e. in the upper-right corner of figure 5*a*).

This experiment can be qualitatively compared to the theoretical prediction (3.1), where the amplitude of this latter is fitted on the experiments (figure 5*b*). Overall, this comparison is promising. However, the capillary wave packet is not present in the prediction, which is expected since only long standing Faraday waves were considered in (3.1). This latter also predicts waves of finite amplitude everywhere on the bath at

https://doi.org/10.1017/jfm.2018.358 Published online by Cambridge University Press

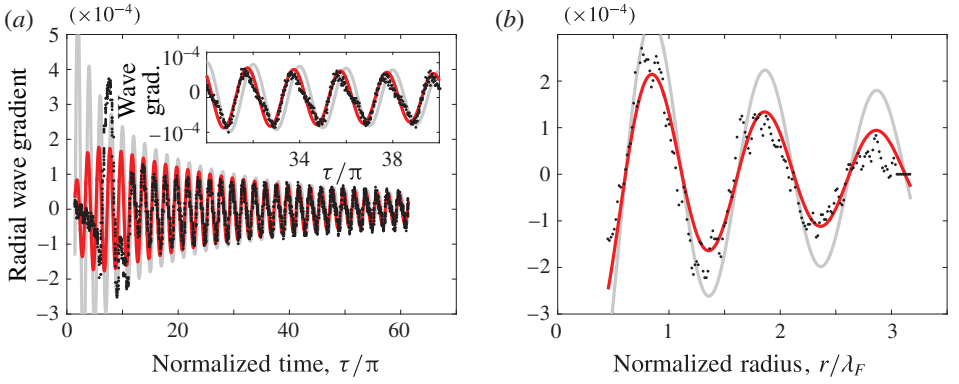


FIGURE 6. (Colour online) Radial gradient of surface waves, (*a*) versus time at a fixed distance $r = 1.32$ cm from the impact, and (*b*) versus position at a fixed time, $t = 0.233$ s after impact. The experimental data are a subset of those represented in figure 5(*a*). Black dots correspond to the gradient measured experimentally. The grey and red solid curves correspond to (1.5) and (3.1), respectively. The inset in (*a*) is a zoom of the main graph on a smaller time window. The present model (red curve) predicts a phase shift of $+\pi/4$ between the Faraday waves and the forcing signal, which is in better agreement with experiments than previous models (grey curve).

$t > t_i$, independently of the passage of the capillary wave packet, which was hard to observe experimentally. Nevertheless, their amplitude remains very small shortly after impact and far from the impact point, which may be the reason why the bath appears still this region of the experimental spatio-temporal diagram.

A more quantitative comparison is provided in figure 6(*a*,*b*), where the radial gradient of the wave is represented as a function of time (at a given position), and as a function of space (at a given time), respectively. The theoretical prediction (3.1) of long-lived Faraday waves is compared to both experiments and the previous model of Moláček & Bush (2013) (given by the gradient of (1.5)). The amplitude factors (v_F in (3.1), and $A \sin \Phi$ in (1.5)) are fitted to the experimental data in the region (r, t) that corresponds to the space–time domain after the passage of the capillary wave packet.

In figure 6(*a*), it is seen that both models capture well the long-term evolution of the wave at a given position. Nevertheless, a zoom on a small time window (inset of figure 6*a*) reveals that the factor $\cos(\Omega t/2 + \pi/4)$ of (3.1) fits experimental data better than the factor $\cos(\Omega t/2)$ of (1.5). In the short-term regime (i.e. before the passage of the capillary wave packet), the experimental wave amplitude is very small. None of the models accurately capture this behaviour, although the addition of short-lived waves in (3.1) might improve the prediction. However, equation (1.5) diverges at short times, while equation (3.1) grows from zero according to an exponential–diffusive behaviour, which is much more realistic. Moreover in (1.5), the information of impact is immediately transmitted everywhere on the bath. By contrast, the present theory predicts that after an impact the bath is first quiet and destabilises progressively owing to diffusive spreading.

The radial evolution of the wave at a given time, seen in figure 6(*b*), is qualitatively similar for both models and experiment. Nevertheless, the spatial damping predicted by (3.1) is closer to experiments than the one of (1.5).

https://doi.org/10.1017/jfm.2018.358 Published online by Cambridge University Press

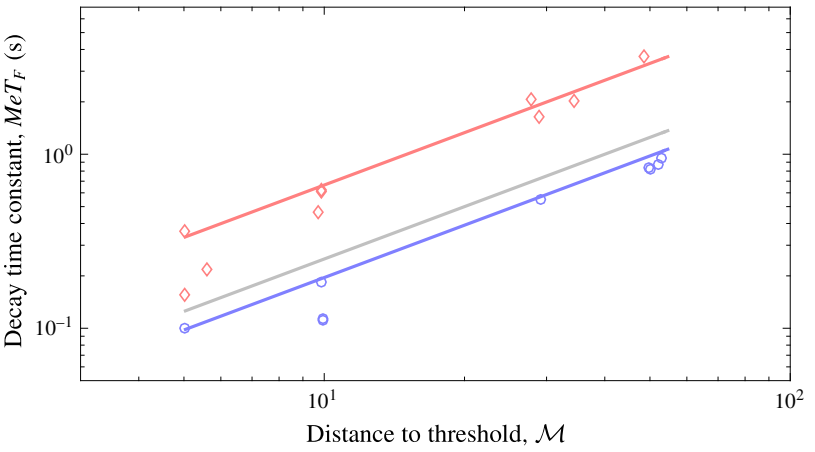


FIGURE 7. (Colour online) Temporal damping MeT_F, as a function of the distance to threshold $\mathcal{M}$. Red diamonds (◇) and blue circles (○) correspond to experiments with silicone oil of viscosity 5 cS and 20 cS, respectively. Red and blue solid lines correspond to (2.65) with the corresponding viscosity. The grey line represents $MeT_F = \mathcal{M}$.

The temporal damping of Faraday waves (envelope of the curve in figure 6*a*) was already observed by Eddi *et al.* (2011). It was then interpreted as the memory Me of the waves, which revealed to be a crucial parameter for the dynamics of walkers (Bush 2015). However, the definition given by Eddi *et al.* (2011) differs from (2.65), as the former is independent of viscosity while the latter is inversely proportional to viscosity in first approximation. In order to validate (2.40), we have measured the damping time MeT_F as a function of the distance to threshold $\mathcal{M}$ for two different silicone oils, of kinematic viscosity 5 cS and 20 cS respectively (figure 7). The comparison with the theoretical prediction (2.65) is excellent. In particular MeT_F is proportional to $\mathcal{M}$ and inversely proportional to viscosity.

3.3. *Wave amplitude versus impact phase*

The amplitude of the Faraday waves generated by an impact is reported for different phases of impact $\tau_i = t_i\Omega/2$ in figure 8. This amplitude is measured as the experimental envelope of $\partial_r\zeta(r, t)$ at a particular location r and time t. It varies sinusoidally with τ_i, so there are some impact phases for which the long-term excited wave is almost non-existent. Our model (3.1) predicts a dependence in $\cos(\tau_i - \pi/4)$ which is qualitatively similar. However, a dependence in $\cos(\tau_i + \pi/5)$ would correspond much better to the measurements.

This phase shift between experiments and theory is likely due to the fact that (3.1) represents an impulse response of surface waves, while in experiments the penetration of the bead into the bath is not instantaneous. According to Duhamel's principle, the response to the bead impact can be calculated by convolving the impulse response with the sophisticated pressure signal $\Pi_k(\tau)$ applied by the bead on the bath. This convolution is expected to approximately shift the effective impact time by half the time of penetration, which is of the order of the contact time $5\sqrt{\rho R_d^3/\sigma} \sim 12$ ms for a bead of radius $R_d = 0.5$ mm (Molacek & Bush 2013). On the other hand, the time delay corresponding to a phase shift from $-\pi/4$ to $\pi/5$ is 5.625 ms, which is very close to the 6 ms that such convolution would predict.

https://doi.org/10.1017/jfm.2018.358 Published online by Cambridge University Press

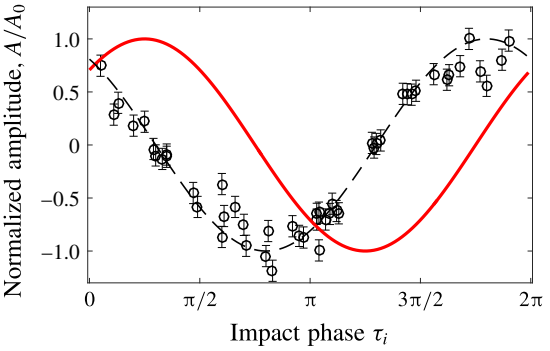


FIGURE 8. (Colour online) Amplitude of the Faraday waves gradient, normalised with $A_0 = 1.9 \times 10^{-4}$ (at fixed position $r = 1.32$ cm and time $t = 0.233$ s), as a function of impact phase τ_i. Symbols correspond to experimental data with oil viscosity $\nu = 20$ cS, $\Omega = 80 \times 2\pi$ s^{-1} and $\mathcal{M} = 30$. The red curve is the theoretical prediction $\cos(\tau_i - \pi/4)$ from the impulse response (3.1) while the black dashed line is $\cos(\tau_i + \pi/5)$.

4. Discussion and conclusion

In § 2, we introduced a theory for the Faraday instability derived from Navier–Stokes equations and based on the only assumption that the surface waves are linear and purely subharmonic. This assumption allows us to truncate the Floquet series (2.26), and it is valid when $\Gamma \lesssim \Gamma_F$ (i.e. close to the Faraday threshold) for wavenumbers $k \simeq k_F$. We have then calculated the dispersion relation of Faraday waves, the Faraday threshold Γ_F and the Faraday wavenumber, k_F. We have shown that for $\Gamma \lesssim \Gamma_F$, there is a range of k in the vicinity of k_F, called the Faraday window, in which the frequency is locked to half the driving frequency (subharmonic response). Waves within this window are standing Faraday waves, while waves outside this window are dispersive travelling waves. The Faraday waves are long lived, and their damping time is proportional to the so-called distance to threshold $\mathcal{M} = \Gamma_F/(\Gamma_F - \Gamma)$, as already observed in previous studies (Eddi *et al.* 2011). The present theory further predicts (see (2.65)) that the damping time is approximately inversely proportional to the fluid viscosity.

The impulse response of the surface waves has been calculated in § 2.3. Similarly to previous models (e.g. (Eddi *et al.* 2011; Moláček & Bush 2013; Milewski *et al.* 2015)), its spatial dependence involves a Bessel function $\mathrm{J}_0(k_F r)$ and its time evolution is a damped oscillation at frequency $\Omega/2$ (subharmonic response). Some of these previous models refer to a similar exponential damping in space. We show here that this damping is not strictly present in the impulse response. Instead, the wave amplitude is modulated by an exponential whose argument scales as $-r^2/(\tau - \tau_i)$. This modulation captures the diffusive propagation of the impulse excitation to the entire bath. A direct consequence is that two walkers do not instantly feel the impacts of each other. The time oscillation of the waves is phase shifted by $\pi/4$ compared to the shaker signal. In other terms, the wave elevation $\zeta(r, t)$ is identically zero when the shaker is at its lowest position. This phase shift, confirmed experimentally, may significantly affect the vertical bouncing dynamics of the walker. Indeed, when the droplet impacts the bath, it feels an absolute acceleration that corresponds to the sum of contributions from the shaker motion and from the overlying phase-shifted Faraday waves.

https://doi.org/10.1017/jfm.2018.358 Published online by Cambridge University Press

Experiment	V_w (mm s^{-1})	$\sqrt{2}d$ (mm)	$\mathcal{M}$	$MeT_F V_w/\sqrt{2}d$	$l/\sqrt{2}d$	R/l
Couder & Fort (2006)	18.9	20.2	5–20	0.12–0.5	0.8	2.5–4.7
Andersen *et al.* (2015)	15	14	21	0.5	1.17	2.82
Pucci *et al.* (2018)	12	28.3	500	5.3	2.18	1.15

TABLE 2. Experimental conditions used in three previous double-slit experiments with walkers (Couder & Fort 2006; Andersen *et al.* 2015; Pucci *et al.* 2018). Walking speed V_w, path length of the waves $\sqrt{2}d$, distance to threshold $\mathcal{M}$, normalised damping time $MeT_F V_w/\sqrt{2}d$, normalised damping length $l/\sqrt{2}d$ and normalised distance to boundaries R/l.

The wave field of a walker can be constructed by adding impulse responses corresponding to each impact of the droplet. This calculation has here been done in the case of a single walker moving at constant speed along a straight line. Under these assumptions, the vertical bouncing motion is perfectly periodic, and all impulse responses are given the same weight. However, the amplitude of the impulse response is modulated according to the phase of impact τ_i relative to the shaker, as predicted by this theory and confirmed experimentally. We expect the vertical dynamics of the walker to be perturbed as soon as additional Faraday waves are present. These Faraday waves may originate from the presence of other walkers, from the vicinity of a boundary, or from a previous passage of the walker at the same location (in the case of very high memory). In each of these cases, the vertical dynamics is not strictly periodic. Consequently, impact phase variations must be taken into account in the construction of the resulting wave field through an appropriately weighted summation of impulse responses. These refinements of the temporal description of Faraday waves are likely to be an additional source of chaos in the dynamics of walkers.

The wave of a regular walker is shown to be at least exponentially damped in space. The characteristic damping length $l(\theta)$ is calculated (while it was experimentally estimated in previous works, e.g. in Eddi *et al.* (2011)). It increases with $\mathcal{M}$ and reaches a finite asymptotic value for $\mathcal{M} \to \infty$. It also decreases with increasing speed or viscosity. This damping length plays a crucial role for the walker dynamics, especially in the landmark double-slit experiment initially performed with walkers by Couder & Fort (2006) and latter contested by Andersen *et al.* (2015). In this experiment, a walking droplet passing to one slit has to possibly interfere with the waves that it sends to the other slit. Such interference is only possible if the waves emitted by the droplet before it crosses the slits are still significantly present when they are received by the droplet beyond the slits. This requires the damping time to be larger than the time required to cross the slits, and the damping length should then be significantly larger than the path length that they have to travel. If the slits are separated by a distance d, the damping length should then be larger than $\sqrt{2}d$. Experimental conditions of Couder & Fort (2006), Andersen *et al.* (2015), Pucci *et al.* (2018) are reported in table 2. As a matter of fact, none of them, except the very recent one of Pucci *et al.* (2018), satisfied the two conditions for significant interferences: the damping time was always lower than the time to cross the slit, and the damping length was not much larger than d. In order to possibly observe interference patterns with single walkers, one would have to reproduce this experiment with a significantly higher memory (i.e. closer to Faraday threshold) and with a fluid

https://doi.org/10.1017/jfm.2018.358 Published online by Cambridge University Press

of significantly lower viscosity. Boundaries other than those that generate the expected diffraction must be placed farther than the damping length. So for example, the radius R of the reservoir must satisfy $R \gg l$, which was not the case in the work of Pucci *et al.* (2018). More generally, the damping length represents the distance at which the walker can probe its surrounding, would there be a boundary or other walkers. It is therefore a crucial parameter to the investigation of many other experiments on walkers, including those involving surreal trajectories, tunnelling or interactions between several walkers.

By contrast with walkers and Faraday waves, quantum mechanics is intrinsically non-dissipative. This feature can conceptually be approached with the walkers, by considering the limit of vanishing viscosity. In appendix F, we show that the waves generated by walkers remain linear in this limit, even though the thickness of the viscous boundary layer decreases to zero. In § 2.5, we have provided developments in series in the low-viscosity limit. If viscosity vanished (i.e. here $\gamma_0 \to 0$), the Faraday threshold Γ_F would vanish too, so the amplitude of the required driving vibration could be arbitrarily small. The memory Me would diverge and excitations from the bouncing droplets would be remembered by the wave forever. The diffusion coefficient D and the damping length l would diverge too, so each droplet impact would instantly modify the whole bath surface (with the compressibility of the liquid as a limit), i.e. each walker would instantly feel the presence of others, no matter how far away they are. Therefore, in the limit of vanishing viscosity, walkers become intrinsically non-local objects composed of a local particle coupled to a non-local wave field.

Walkers currently represent the only realisation at the macroscopic scale of a pilot-wave system similar to the one proposed by de Broglie (1987) to interpret quantum mechanics (Bush 2015). Many phenomena initially thought to be specific to the quantum realm have been observed with these walkers. The theory of Faraday waves developed in this paper brings a rigorous framework for the modelling of the wave field generated by a walker. It comprises additions to the previous Faraday wave models that are essential to the description of walkers interfering with others, with boundaries or with their past. It also provides insights on the locality of a walker, which has to be understood before experiments on the possible entanglement of two walkers could potentially be imagined. We hope that that this paper will help the building of a consistent wave theory to describe walkers similarly to Schrödinger's equation for quantum objects. It would then better reveal the limits of the analogy between walkers and the quantum world.

Acknowledgements

The authors thank N. Sampara and B. Begasse for their help in building the experiment, as well as R. Dubertrand and W. Struyve for fruitful discussions. This work was financially supported by the 'Actions de Recherches Concertees (ARC)' of the Belgium Wallonia Brussels Federation under contract No. 12-17/02 and by the FNRS grant number CHAR. RECH.-1.B423.18 (Tadrist L.).

Appendix A. Truncation of the Floquet ansatz

The (2.20) of surface waves in the absence of external pressure $\Pi_k = 0$ is recalled here:

$$f_k(s)\zeta_{k,s} + \frac{2\Gamma gk}{\Omega^2}(\zeta_{k,s+2\mathrm{i}} + \zeta_{k,s-2\mathrm{i}}) = 0. \tag{A 1}$$

https://doi.org/10.1017/jfm.2018.358 Published online by Cambridge University Press

It can be solved with the Floquet ansatz (2.27):

$$\zeta_{k,s} = \sum_{l=-\infty}^{\infty} \frac{\zeta_k^{(l)}}{s-(2l-1)\mathrm{i}}, \tag{A 2}$$

which directly implies that

$$\zeta_{k,s\pm 2\mathrm{i}} = \sum_{l=-\infty}^{\infty} \frac{\zeta_k^{(l)}}{s\pm 2\mathrm{i}-(2l-1)\mathrm{i}} = \sum_{l=-\infty}^{\infty} \frac{\zeta_k^{(l\mp 1)}}{s-(2l-1)\mathrm{i}}. \tag{A 3}$$

Substitution of (A 2) and (A 3) in (A 1) yields

$$\sum_{l=-\infty}^{\infty} \frac{1}{s-(2l-1)\mathrm{i}} \left(f_k(s)\zeta_k^{(l)} + \frac{2\Gamma gk}{\Omega^2}(\zeta_k^{(l-1)} + \zeta_k^{(l+1)}) \right) = 0. \tag{A 4}$$

The Heaviside cover-up method is then applied to obtain a linear system of infinite dimension for the Floquet coefficients $\zeta_k^{(l)}$:

$$\forall l \in \mathbb{Z}, \quad f_k((2l-1)\mathrm{i})\zeta_k^{(l)} + \frac{2\Gamma gk}{\Omega^2}(\zeta_k^{(l-1)} + \zeta_k^{(l+1)}) = 0, \tag{A 5}$$

or in matrix form

$$\underbrace{\begin{pmatrix} \ddots & \ddots & \ddots & 0 & 0 & 0 & 0 & 0 \\ 0 & \alpha & f(-3\mathrm{i}) & \alpha & 0 & 0 & 0 & 0 \\ 0 & 0 & \alpha & f(-\mathrm{i}) & \alpha & 0 & 0 & 0 \\ 0 & 0 & 0 & \alpha & f(\mathrm{i}) & \alpha & 0 & 0 \\ 0 & 0 & 0 & 0 & \alpha & f(3\mathrm{i}) & \alpha & 0 \\ 0 & 0 & 0 & 0 & 0 & \ddots & \ddots & \ddots \end{pmatrix}}_{K} \begin{pmatrix} \vdots \\ \zeta^{(-1)} \\ \zeta^{(0)} \\ \zeta^{(1)} \\ \zeta^{(2)} \\ \vdots \end{pmatrix} = \begin{pmatrix} \vdots \\ 0 \\ 0 \\ 0 \\ 0 \\ \vdots \end{pmatrix}, \tag{A 6}$$

where we denoted $\alpha = 2\Gamma gk/\Omega^2$ for readability. The matrix is tridiagonal, which indicates that each Floquet mode is coupled to its neighbour modes. The condition of existence of surface waves is bound to the obtention of a non-trivial solution to this system. This can only be achieved when the determinant $\det K = 0$, which yields the threshold Γ_k associated with each wavenumber k for the non-truncated Floquet ansatz.

In the main text, we truncated the series to the two first modes, which led to (2.29) and (2.30). The approximation of this truncation may be evaluated by considering the presence of the two next modes. With a truncation enlarged to four modes, the linear system becomes

$$\begin{pmatrix} f_k(-3\mathrm{i}) & \alpha & 0 & 0 \\ \alpha & f_k(-\mathrm{i}) & \alpha & 0 \\ 0 & \alpha & f_k(\mathrm{i}) & \alpha \\ 0 & 0 & \alpha & f_k(3\mathrm{i}) \end{pmatrix} \begin{pmatrix} \zeta^{(-1)} \\ \zeta^{(0)} \\ \zeta^{(1)} \\ \zeta^{(2)} \end{pmatrix} = \begin{pmatrix} 0 \\ 0 \\ 0 \\ 0 \end{pmatrix}. \tag{A 7}$$

A non-trivial solution is found when the determinant is zero, i.e.

$$\frac{\alpha^4}{|f_k(3\mathrm{i})|^2} - \alpha^2 \left(1 + \frac{f_k(-\mathrm{i})}{f_k(3\mathrm{i})} + \frac{f_k(\mathrm{i})}{f_k(-3\mathrm{i})} \right) + |f_k(\mathrm{i})|^2 = 0. \tag{A 8}$$

https://doi.org/10.1017/jfm.2018.358 Published online by Cambridge University Press

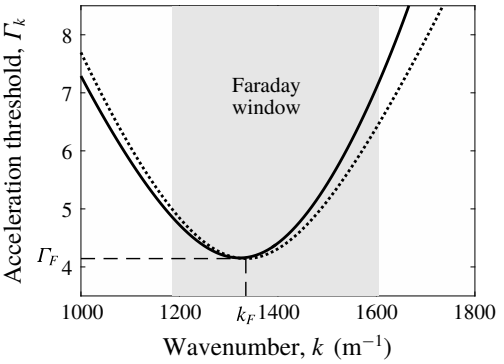


FIGURE 9. Faraday threshold Γ_k of each wavenumber k. The dashed line represents a truncation to the two first modes. The solid line corresponds to the truncation to either four or twenty modes – which are indistinguishable from each other.

The curve Γ_k is given by the smallest positive solution to this equation, namely,

$$\frac{\alpha}{|f_k(3\mathrm{i})|} = \frac{1}{\sqrt{2}}\sqrt{\left(1+\frac{f_k(-\mathrm{i})}{f_k(3\mathrm{i})}+\frac{f_k(\mathrm{i})}{f_k(-3\mathrm{i})}\right) - \sqrt{\left(1+\frac{f_k(-\mathrm{i})}{f_k(3\mathrm{i})}+\frac{f_k(\mathrm{i})}{f_k(-3\mathrm{i})}\right)^2 - 4\frac{|f_k(\mathrm{i})|^2}{|f_k(3\mathrm{i})|^2}}}. \tag{A 9}$$

Around k_F, in the low-viscosity limit (cf. appendix B), one can show that for $k \sim k_F$, $|f_k(\mathrm{i})|^2 \sim 4\gamma_k^2$ and $|f_k(3\mathrm{i})|_F^2 \sim 64$. Consequently, $|f(\mathrm{i})|_F^2/|f(3\mathrm{i})^2|_F \sim \gamma_F^2/16 \ll 1$. Equation (A 9) can then be expanded in Taylor series, which yields

$$\Gamma_k = \frac{\Omega^2|f_k(\mathrm{i})|}{2gk}\left(1-\frac{|f_k(\mathrm{i})|^2}{2|f_k(3\mathrm{i})|^2}\frac{1}{(1+f_k(-\mathrm{i})/f_k(3\mathrm{i})+f_k(\mathrm{i})/f_k(-3\mathrm{i}))^2}\right). \tag{A 10}$$

The correction to Γ_k corresponding to the addition of four terms instead of two in the Floquet ansatz is of the order of $|f(\mathrm{i})|^2/2|f(3\mathrm{i})|^2 \sim \gamma_F^2/32 < 1\,\%$ in the limit of small viscosity and for $k \sim k_F$.

Figure 9 represents the curve Γ_k, calculated with a truncation to 2 modes, to 4 modes and to 20 modes respectively. The first two modes already provide a very good estimation of the curve Γ_k, especially for $k \simeq k_F$. The curves Γ_k for four and twenty modes are almost indistinguishable. For walker parameters (cf. table 1), $\Gamma_F = 4.155$ with a truncation to 20 modes whereas $\Gamma_F = 4.144$ with a truncation to only 2 modes. Similarly, the Faraday wavelength is $\lambda_F = 4.749$ mm with 20 modes, instead of $\lambda_F = 4.706$ with two modes. In both cases, the relative error from the truncation to two modes is less than 1 %.

Appendix B. Low-viscosity asymptotic behaviour

B.1. *Preliminary calculations*

The function f_k and its derivatives are first recalled:

$$f_k(s) = (s+\gamma_k)^2 + \omega_k^2 - \gamma_k^{3/2}\sqrt{\gamma_k + 2s}, \tag{B 1}$$

https://doi.org/10.1017/jfm.2018.358 Published online by Cambridge University Press

$$\dot{f}_k(s) = 2(s+\gamma_k) - \frac{\gamma_k^{3/2}}{\sqrt{\gamma_k+2s}}, \tag{B 2}$$

$$\ddot{f}_k(s) = 2 + \left(\frac{\gamma_k}{\gamma_k+2s}\right)^{3/2}. \tag{B 3}$$

They are all self-conjugated, so e.g. $f_k(s^*) = f_k(s)^*$.

In order to evaluate them in $s = \pm i$, we first calculate

$$\sqrt{\gamma_k \pm 2\mathrm{i}} = \frac{1}{\sqrt{2}}\sqrt{\sqrt{\gamma_k^2+4}+\gamma_k} \pm \frac{\mathrm{i}}{\sqrt{2}}\sqrt{\sqrt{\gamma_k^2+4}-\gamma_k}. \tag{B 4}$$

Only the positive real part is considered, since the vertical fluid velocity must remain finite when $z \longrightarrow -\infty$ in (2.19).

Therefore, without any approximation,

$$\mathrm{Re}(f_k(\mathrm{i})) = \gamma_k^2 + \omega_k^2 - 1 - \frac{\gamma_k^{3/2}}{\sqrt{2}}\sqrt{\sqrt{\gamma_k^2+4}+\gamma_k}, \tag{B 5}$$

$$\mathrm{Im}(f_k(\mathrm{i})) = 2\gamma_k - \frac{\gamma_k^{3/2}}{\sqrt{2}}\sqrt{\sqrt{\gamma_k^2+4}-\gamma_k}, \tag{B 6}$$

$$\mathrm{Re}(\dot{f}_k(\mathrm{i})) = 2\gamma_k - \frac{\gamma_k^{3/2}}{\sqrt{2}\sqrt{\gamma_k^2+4}}\sqrt{\sqrt{\gamma_k^2+4}+\gamma_k}, \tag{B 7}$$

$$\mathrm{Im}(\dot{f}_k(\mathrm{i})) = 2 + \frac{\gamma_k^{3/2}}{\sqrt{2}\sqrt{\gamma_k^2+4}}\sqrt{\sqrt{\gamma_k^2+4}-\gamma_k}, \tag{B 8}$$

$$\mathrm{Re}(\ddot{f}_k(\mathrm{i})) = 2 + \frac{\gamma_k^{3/2}}{\sqrt{2}(\gamma_k^2+4)^{3/2}}\left(\gamma_k\sqrt{\sqrt{\gamma_k^2+4}+\gamma_k} - 2\sqrt{\sqrt{\gamma_k^2+4}-\gamma_k}\right), \tag{B 9}$$

$$\mathrm{Im}(\ddot{f}_k(\mathrm{i})) = -\frac{\gamma_k^{3/2}}{\sqrt{2}(\gamma_k^2+4)^{3/2}}\left(\gamma_k\sqrt{\sqrt{\gamma_k^2+4}-\gamma_k} + 2\sqrt{\sqrt{\gamma_k^2+4}+\gamma_k}\right). \tag{B 10}$$

When the viscosity is sufficiently small, $\gamma_k \ll 1$, and both $f_k(i)$ and its derivatives can be approximated with a Taylor series in γ_k:

$$\mathrm{Re}(f_k(\mathrm{i})) = \omega_k^2 - 1 - \gamma_k^{3/2} + \gamma_k^2 - \frac{1}{4}\gamma_k^{5/2} + O(\gamma_k^{7/2}), \tag{B 11}$$

$$\mathrm{Im}(f_k(\mathrm{i})) = 2\gamma_k - \gamma_k^{3/2} + \frac{1}{4}\gamma_k^{5/2} + O(\gamma_k^{7/2}), \tag{B 12}$$

$$\mathrm{Re}(\dot{f}_k(\mathrm{i})) = 2\gamma_k - \frac{\gamma_k^{3/2}}{2} - \frac{\gamma_k^{5/2}}{8} + O(\gamma_k^{7/2}), \tag{B 13}$$

$$\mathrm{Im}(\dot{f}_k(\mathrm{i})) = 2 + \frac{\gamma_k^{3/2}}{2} - \frac{\gamma_k^{5/2}}{8} + O(\gamma_k^{7/2}), \tag{B 14}$$

$$\mathrm{Re}(\ddot{f}_k(\mathrm{i})) = 2 - \frac{\gamma_k^{3/2}}{4} + \frac{3}{16}\gamma_k^{5/2} + O(\gamma_k^{7/2}), \tag{B 15}$$

$$\mathrm{Im}(\ddot{f}_k(\mathrm{i})) = -\frac{\gamma_k^{3/2}}{4} - \frac{3}{16}\gamma_k^{5/2} + O(\gamma_k^{7/2}). \tag{B 16}$$

https://doi.org/10.1017/jfm.2018.358 Published online by Cambridge University Press

The following combinations of $f_k(\mathrm{i})$ and its derivatives are regularly called in § 2:

$$|f_k(\mathrm{i})|^2 = (\omega_k^2-1)^2 - 2(\omega_k^2-1)\gamma_k^{3/2} + 2(\omega_k^2+1)\gamma_k^2 - \left(4+\frac{\omega_k^2-1}{2}\right)\gamma_k^{5/2} + 2\gamma_k^3 + O(\gamma_k^{7/2}), \tag{B 17}$$

$$f_k(\mathrm{i})\dot{f}_k(-\mathrm{i}) + f_k(-\mathrm{i})\dot{f}_k(\mathrm{i}) = 4\gamma_k(\omega_k^2+1) - (\omega_k^2+3)\gamma_k^{3/2} - \left(\frac{\omega_k^2+3}{4}\right)\gamma_k^{5/2} + O(\gamma_k^3), \tag{B 18}$$

$$\frac{f_k(\mathrm{i})\ddot{f}_k(-\mathrm{i}) + f_k(-\mathrm{i})\ddot{f}_k(\mathrm{i})}{2} + \dot{f}_k(\mathrm{i})\dot{f}_k(-\mathrm{i}) = 2(\omega_k^2+1) - \frac{\omega_k^2-1}{4}\gamma_k^{3/2} + 6\gamma_k^2 + \frac{3\omega_k^2-59}{16}\gamma_k^{5/2} + O(\gamma_k^{7/2}). \tag{B 19}$$

Finally, the two first k-derivative of $|f_k(\mathrm{i})|^2$, useful for the calculation of the Faraday threshold and the diffusion coefficient, are expanded as:

$$\frac{k}{2}\frac{\partial|f_k(\mathrm{i})|^2}{\partial k} = 2k(\omega_k^2-1)\omega_k c_k - (2k\omega_k c_k + 3(\omega_k^2-1))\gamma_k^{3/2} + (2k\omega_k c_k + 4(\omega_k^2+1))\gamma_k^2 - \left[\frac{k\omega_k c_k}{2} + \frac{5}{2}\left(4+\frac{\omega_k^2-1}{2}\right)\right]\gamma_k^{5/2} + 6\gamma_k^3 + O(\gamma_k^{7/2}), \tag{B 20}$$

$$\frac{\partial^2|f_k(\mathrm{i})|^2}{\partial k^2} = 8\omega_k^2 c_k^2 + 4(\omega_k^2-1)(c_k^2+\omega_k\dot{c}_k) - \left(4(c_k^2+\omega_k\dot{c}_k) + \frac{12}{k^2}(\omega_k^2-1) + \frac{24\omega_k c_k}{k}\right)\gamma_k^{3/2} + O(\gamma_k^2), \tag{B 21}$$

where $c_k = \partial\omega_k/\partial k$ is the dimensionless group velocity, and $\dot{c}_k = \partial c_k/\partial k$.

The low-viscosity approximation of the damping of Faraday waves reads

$$\delta_k^+ = -\frac{\left((\omega_k^2-1)^2 - 2(\omega_k^2-1)\gamma_k^{3/2} + 2(\omega_k^2+1)\gamma_k^2 - \left(4+\frac{\omega_k^2-1}{2}\right)\gamma_k^{5/2} - (2\Gamma gk/\Omega^2)^2\right)}{4(\omega_k^2+1)\gamma_k - (\omega_k^2+3)\gamma_k^{3/2} - (\omega_k^2+3)\gamma_k^{5/2}/4} + O(\gamma_k^3). \tag{B 22}$$

B.2. *Determination of k_F, ω_F and c_F*

The most unstable wavenumber k_F is defined as the solution of

$$\frac{k}{2}\frac{\partial|f_k(\mathrm{i})|^2}{\partial k} = |f_k(\mathrm{i})|^2. \tag{B 23}$$

According to the approximations (B 17) and (B 20), it satisfies

$$(\omega_F^2-1)(\omega_F^2-1-2k_F\omega_F c_F) + (\omega_F^2-1+2k_F\omega_F c_F)\gamma_F^{3/2} - (2(\omega_F^2+1)+2k_F\omega_F c_F)\gamma_F^2 + \left(6+\frac{3}{4}(\omega_F^2-1)+\frac{k_F\omega_F c_F}{2}\right)\gamma_F^{5/2} - 4\gamma_F^3 + O(\gamma_F^{7/2}) = 0, \tag{B 24}$$

where $\omega_F = \omega_{k_F}$ and $c_F = c_{k_F}$.

https://doi.org/10.1017/jfm.2018.358 Published online by Cambridge University Press

When the viscosity ν is identically zero, $\gamma_F = 0$ and (B 24) is simplified

$$(\omega_F^2 - 1)(\omega_F^2 - 1 - 2k_F\omega_F c_F) = 0. \tag{B 25}$$

The second factor is strictly negative for $k_F > 0$, so k_F must satisfy $\omega_F^2 = 1$. We define

$$k_0 = \lim_{\nu \to 0} k_F \tag{B 26}$$

for which $\omega_0 = \omega_{k_0} = 1$, $c_0 = c_{k_0}$ and $\gamma_0 = \gamma_{k_0}$.

The damping factor $\gamma_0 = 4\nu k_0^2/\Omega$ is a better basis for an asymptotic expansion at low viscosity, since it does not directly depend on the Faraday wavenumber k_F, which is still unknown. Equation (B 24) can be rewritten in terms of γ_0 since $\gamma_F = k_F^2\gamma_0/k_0^2$:

$$\begin{aligned}&(\omega_F^2 - 1)(\omega_F^2 - 1 - 2k_F\omega_F c_F) + (\omega_F^2 - 1 + 2k_F\omega_F c_F)\left(\frac{k_F}{k_0}\right)^3 \gamma_0^{3/2} \\ &- (2(\omega_F^2 + 1) + 2k_F\omega_F c_F)\left(\frac{k_F}{k_0}\right)^4 \gamma_0^2 + \left(6 + \frac{3}{4}(\omega_F^2 - 1) + \frac{k_F\omega_F c_F}{2}\right)\left(\frac{k_F}{k_0}\right)^5 \gamma_0^{5/2} \\ &- 4\left(\frac{k_F}{k_0}\right)^6 \gamma_0^3 + O(\gamma_0^{7/2}) = 0.\end{aligned} \tag{B 27}$$

We formulate the ansatz

$$k_F = k_0 + \epsilon\gamma_0^\alpha + o(\gamma_0^\alpha), \tag{B 28}$$

where $\alpha > 0$, from which we directly infer that

$$\omega_F^2 = 1 + 2c_0\epsilon\gamma_0^\alpha + o(\gamma_0^\alpha) \tag{B 29}$$

and

$$2\omega_F c_F = 2c_0 + \frac{24\sigma}{\rho\Omega^2}k_0\epsilon\gamma_0^\alpha + o(\gamma_0^\alpha). \tag{B 30}$$

Inserting this ansatz in (B 27) yields

$$2c_0k_0(\gamma_0^{3/2} - 2c_0\epsilon\gamma_0^\alpha) + o(\gamma^\alpha) + o(\gamma^{3/2}) = 0 \tag{B 31}$$

from which we deduce $\alpha = 3/2$ and $\epsilon = 1/(2c_0)$, so $k_F = k_0 + (1/2c_0)\gamma_0^{3/2} + o(\gamma_0^{3/2})$. We can iterate this procedure with a new ansatz $k_F = k_0 + \gamma_0^{3/2}/(2c_0) + \epsilon\gamma_0^\alpha + o(\gamma_0^\alpha)$ in order to find higher-order corrections. This yields:

$$\left.\begin{aligned} k_F &= k_0 + \frac{1}{2c_0}\gamma_0^{3/2} - \frac{2 + k_0c_0}{2k_0c_0^2}\gamma_0^2 + \frac{12 + k_0c_0}{8k_0c_0^2}\gamma_0^{5/2} + \left(\frac{1}{4k_0c_0^2} - \frac{d_0}{8c_0^3}\right)\gamma_0^3 + O(\gamma_0^{7/2}), \\ \omega_F^2 &= 1 + \gamma_0^{3/2} - \frac{2 + k_0c_0}{k_0c_0}\gamma_0^2 + \frac{12 + k_0c_0}{4k_0c_0}\gamma_0^{5/2} + O(\gamma_0^3), \\ \gamma_F &= \gamma_0 + \frac{\gamma_0^{5/2}}{k_0c_0} + O(\gamma_0^3), \end{aligned}\right\} \tag{B 32}$$

where $d_0 = (\partial^2\omega_k^2/\partial k^2)(k_0)$.

https://doi.org/10.1017/jfm.2018.358 Published online by Cambridge University Press

From there, we evaluate:

$$\left.\begin{aligned}
\mathrm{Re}(f_F(\mathrm{i})) &= \frac{-2}{k_0c_0}\gamma_0^2 + \frac{3}{k_0c_0}\gamma_0^{5/2} + O(\gamma_0^3),\\
\mathrm{Im}(f_F(\mathrm{i})) &= 2\gamma_0 - \gamma_0^{3/2} + \frac{8+k_0c_0}{4k_0c_0}\gamma_0^{5/2} + O(\gamma_0^3),\\
f_F(\mathrm{i})\dot{f}_F(-\mathrm{i}) + f_F(-\mathrm{i})\dot{f}_F(\mathrm{i}) &= 8\gamma_0 - 4\gamma_0^{3/2} + O(\gamma_0^2),\\
\frac{f_F(\mathrm{i})\ddot{f}_F(-\mathrm{i}) + f_F(-\mathrm{i})\ddot{f}_F(\mathrm{i})}{2} + \dot{f}_F(\mathrm{i})\dot{f}_F(-\mathrm{i}) &= 2\gamma_0^{3/2} + 4\left(1-\frac{1}{k_0c_0}\right)\gamma_0^2\\
&\quad + \frac{12+9k_0c_0}{2k_0c_0}\gamma_0^{5/2} + O(\gamma_0^3),\\
\left.\frac{\partial^2|f_k(\mathrm{i})|^2}{\partial k^2}\right|_F &= 8c_0^2 + O(\gamma_0^{3/2}).
\end{aligned}\right\} \quad \text{(B 33)}$$

Appendix C. Inverse Hankel transform

In this appendix, we evaluate the integral (2.52), namely

$$\zeta_1(r,\tau) = \int_0^\infty B_k^+ \cos(\tau+\theta_k^+)\mathrm{e}^{\delta_k^+(\tau-\tau_i)}\mathrm{J}_0(kr)k\,\mathrm{d}k, \quad \text{(C 1)}$$

with the saddle-node method. First, δ_k^+ is replaced by its Taylor series around k_F:

$$\delta_k^+ \simeq \delta_F - D(k-k_F)^2. \quad \text{(C 2)}$$

Substitution in the integral yields

$$\zeta_1(r,\tau) = \mathrm{e}^{\delta_F(\tau-\tau_i)}\int_0^\infty B_k^+\cos(\tau+\theta_k^+)\mathrm{e}^{-D(\tau-\tau_i)(k-k_F)^2}\mathrm{J}_0(kr)k\,\mathrm{d}k. \quad \text{(C 3)}$$

In the limit $k_Fr \ll 1$, the Bessel function does not oscillate significantly. Then for $\tau \gg \tau_i$,

$$\begin{aligned}
\zeta_1(r,\tau) &\simeq \mathrm{e}^{\delta_F(\tau-\tau_i)}B_F^+\cos(\tau+\theta_F^+)\mathrm{J}_0(k_Fr)k_F\int_0^\infty \mathrm{e}^{-D(\tau-\tau_i)(k-k_F)^2}\,\mathrm{d}k\\
&= B_F^+k_F\mathrm{e}^{\delta_F(\tau-\tau_i)}\cos(\tau+\theta_F^+)\sqrt{\frac{\pi}{D(\tau-\tau_i)}}\mathrm{J}_0(k_Fr). \quad \text{(C 4)}
\end{aligned}$$

For $k_Fr \gg 1$, the approximation of J_0 by $\mathrm{Re}\{\mathrm{e}^{\mathrm{i}kr+\mathrm{i}\pi/4}/\sqrt{\pi kr/2}\}$ yields

$$\begin{aligned}
\zeta_1(r,\tau) &\simeq \mathrm{e}^{\delta_F(\tau-\tau_i)}\int_0^\infty B_k^+\cos(\tau+\theta_k^+)\mathrm{e}^{-D(\tau-\tau_i)(k-k_F)^2}\mathrm{e}^{\mathrm{i}kr+\mathrm{i}\pi/4}\sqrt{\frac{2}{\pi kr}}k\,\mathrm{d}k\\
&\simeq \mathrm{e}^{\delta_F(\tau-\tau_i)}B_F^+\cos(\tau+\theta_F^+)\mathrm{J}_0(k_Fr)k_F\int_0^\infty \mathrm{e}^{-D(\tau-\tau_i)(k-k_F)^2}\mathrm{e}^{\mathrm{i}(k-k_F)r}\,\mathrm{d}k. \quad \text{(C 5)}
\end{aligned}$$

The remaining integral is calculated as

$$\begin{aligned}
\int_0^\infty \mathrm{e}^{-D(\tau-\tau_i)(k-k_F)^2}\mathrm{e}^{\mathrm{i}(k-k_F)r}\,\mathrm{d}k &= \exp\left[-\frac{r^2}{4D(\tau-\tau_i)}\right]\int_0^\infty \mathrm{e}^{-D(\tau-\tau_i)[k-k_F-(\mathrm{i}r)/(2D(\tau-\tau_i))]^2}\,\mathrm{d}k\\
&= \exp\left[-\frac{r^2}{4D(\tau-\tau_i)}\right]\sqrt{\frac{\pi}{D(\tau-\tau_i)}}. \quad \text{(C 6)}
\end{aligned}$$

https://doi.org/10.1017/jfm.2018.358 Published online by Cambridge University Press

Therefore,

$$\zeta_1(r,\tau) \simeq B_F^+ k_F \mathrm{e}^{\delta_F(\tau-\tau_i)} \cos(\tau+\theta_F^+)\sqrt{\frac{\pi}{D(\tau-\tau_i)}}\mathrm{J}_0(k_F r)\exp\left[-\frac{r^2}{4D(\tau-\tau_i)}\right]. \quad \text{(C 7)}$$

Coincidentally, this asymptotic behaviour at $k_F r \gg 1$ is also valid for $k_F r \ll 1$. Indeed, equations (C 4) and (C 7) are identical as soon as $\tau - \tau_i \gg r^2/(4D)$. This condition is necessarily satisfied as soon as $\tau - \tau_i \gg 1/(4Dk_F^2)$ for $k_F r \ll 1$. For walkers, with numerical values in table 1, $1/4Dk_F^2 \sim 0.08$ so (C 7) is equivalently valid at $k_F r \gg 1$ and $k_F r \ll 1$.

Appendix D. Surface waves emitted by a walker

The Faraday wave profile resulting from the previous bounces of the walker at the positions $\boldsymbol{r}_n = -(\tau-\tau_n)\boldsymbol{v}$ and the times $\tau_n = \tau_i + 2\pi n$ $(n \in \mathbb{Z})$ reads

$$\begin{aligned}\zeta_w(\boldsymbol{r},\tau) &= \sum_{n=-\infty}^{[(\tau-\tau_i)/2\pi]} \zeta_1(|\boldsymbol{r}-\boldsymbol{r}_n|,\tau-\tau_n)\\ &= \sum_{n=-\infty}^{[(\tau-\tau_i)/2\pi]} B_F^+ k_F\sqrt{\frac{\pi}{D(\tau-\tau_n)}}\mathrm{J}_0(k_F|\boldsymbol{r}-\boldsymbol{r}_n|)\cos(\tau+\theta_F^+)\\ &\quad\times\exp\left(-\frac{\tau-\tau_n}{2\pi Me}-\frac{|\boldsymbol{r}-\boldsymbol{r}_n|^2}{4D(\tau-\tau_n)}\right),\end{aligned} \quad \text{(D 1)}$$

where $[(\tau-\tau_i)/2\pi]$ denotes the largest integer smaller than $(\tau-\tau_i)/2\pi$, and where the origin $\boldsymbol{r}=0$ is placed at the position of the walker at time τ. We replace the sum in the previous equation by an integration over the delay time $u = \tau - \tau_n$ going from 0 to ∞. This is justified for $Mer^2 \gg 2\pi D$, since the sum can then be seen as an approximate Riemann integral where the interpolated function does not significantly vary over one bin.

The Graf's theorem for zeroth-order Bessel function reads

$$\mathrm{J}_0(k_F|\boldsymbol{r}-\boldsymbol{r}_n|) = \sum_{n=-\infty}^{\infty}\mathrm{J}_n(k_F r)\mathrm{J}_n(k_F r_n)\mathrm{e}^{-\mathrm{i}n\theta} \quad \text{(D 2)}$$

with

$$\theta = \arccos\left(\frac{\boldsymbol{v}\cdot\boldsymbol{r}}{vr}\right). \quad \text{(D 3)}$$

Since Bessel functions are defined as

$$\mathrm{J}_n(k_F r) = \frac{1}{2\pi}\int_{-\pi}^{\pi}\mathrm{d}\varphi\mathrm{e}^{\mathrm{i}k_F r\sin\varphi}\mathrm{e}^{-\mathrm{i}n\varphi} \quad \text{(D 4)}$$

and since $\sum[\mathrm{e}^{\mathrm{i}(\theta-\varphi-\varphi')}]^n = \delta(\theta-\varphi-\varphi')$,

$$\mathrm{J}_0(k_F|\boldsymbol{r}-\boldsymbol{r}_n|) = \frac{1}{2\pi}\int_{-\pi}^{\pi}\exp[\mathrm{i}k_F r\sin(\theta-\varphi)]\exp(-\mathrm{i}k_F r_n\sin\varphi)\,\mathrm{d}\varphi. \quad \text{(D 5)}$$

https://doi.org/10.1017/jfm.2018.358 Published online by Cambridge University Press

Substitution in (D 1) yields

$$\zeta_w(\boldsymbol{r},\tau)=\frac{B_F^+k_F}{2\sqrt{\pi D}}\cos(\tau+\theta_F^+)\int_{-\pi}^{\pi}\mathrm{d}\varphi\exp[\mathrm{i}k_Fr\sin(\theta-\varphi)]$$
$$\times\int_0^{\infty}\frac{1}{\sqrt{u}}\exp\left(-\frac{u}{2\pi Me}-\frac{r^2}{4Du}-\frac{vr\cos\theta}{2D}-\frac{v^2u}{4D}+\mathrm{i}k_Fuv\sin\varphi\right)\mathrm{d}u. \quad (D\,6)$$

Using the identity

$$\int_0^{\infty}\frac{1}{\sqrt{u}}\exp(-\alpha u-\beta/u)\,\mathrm{d}u=\sqrt{\frac{\pi}{\alpha}}\exp(-2\sqrt{\alpha\beta}) \quad (D\,7)$$

for $\mathrm{Re}(\alpha)>0$ and $\beta>0$, we obtain

$$\zeta_w(\boldsymbol{r},\tau)=\frac{B_F^+k_F}{2\sqrt{D}}\cos(\tau+\theta_F^+)\exp\left(-\frac{vr\cos\theta}{2D}\right)$$
$$\times\int_{-\pi}^{\pi}\mathrm{d}\varphi\frac{\exp[\mathrm{i}k_Fr\sin(\theta-\varphi)]}{\sqrt{a-\mathrm{i}k_Fv\sin\varphi}}\exp\left(-\frac{r}{\sqrt{D}}\sqrt{a-\mathrm{i}k_Fv\sin\varphi}\right), \quad (D\,8)$$

where

$$a=\frac{1}{2\pi Me}+\frac{v^2}{4D}. \quad (D\,9)$$

For large a such that $k_Fv/a\ll1$ (for walkers, with numerical values in table 1, this corresponds to a distance to threshold $\mathcal{M}<4.8$), we can justify the approximation

$$\sqrt{a-\mathrm{i}k_Fv\sin\varphi}\simeq\sqrt{a}-\mathrm{i}\frac{k_Fv}{2\sqrt{a}}\sin\varphi. \quad (D\,10)$$

A reverse application of Graf's theorem (D 5) yields

$$\zeta_w(\boldsymbol{r},\tau)=\frac{B_F^+k_F}{2\sqrt{Da}}\cos(\tau+\theta_F^+)\mathrm{J}_0\left(k_F\left|\boldsymbol{r}+\frac{r}{2\sqrt{Da}}\boldsymbol{v}\right|\right)$$
$$\times\exp\left[-\left(\sqrt{\frac{a}{D}}+\frac{v\cos\theta}{2D}\right)r\right], \quad (D\,11)$$

i.e. we obtain a Doppler-shifted Bessel profile which is exponentially attenuated in space. The damping length scale, defined as $l(\theta)$, depends on the orientation θ with respect to the walking direction $\boldsymbol{v}/v$:

$$l(\theta)=\frac{2D}{v\cos\theta+\sqrt{v^2+2D/\pi Me}}. \quad (D\,12)$$

In the special case of a stationary bouncer with $v=0$, we obtain the spatial damping length $l=\sqrt{2\pi MeD}$ which diverges in the limit $Me\to\infty$.

An accurate analytical evaluation of (2.57) in the more general case $k_Fv/a\gtrsim1$ is more involved and beyond the scope of this work. However, we can straightforwardly provide an upper limit for the wave amplitude which holds in any case, namely through the inequality

$$\left|\frac{\zeta_w(\boldsymbol{r},\tau)}{\cos(\tau+\theta_F^+)}\right|\leqslant\frac{\pi B_F^+k_F}{\sqrt{Da}}\exp\left[-\frac{r}{l(\theta)}\right], \quad (D\,13)$$

obtained by substituting $|\mathrm{J}_0(k_F|\boldsymbol{r}-\boldsymbol{r}_n|)|\leqslant1$ within (D 1).

https://doi.org/10.1017/jfm.2018.358 Published online by Cambridge University Press

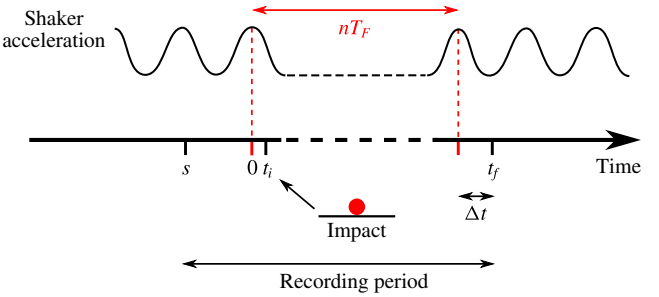


FIGURE 10. (Colour online) Measurement of the impact time t_i, from the end time of the recording t_f and the synchronisation delay Δt. Definitions of t_i, t_f and Δt are provided in the main text.

Appendix E. Experimental measurement of the impact phase

Measuring the impact phase requires a good synchronisation of the high-speed camera with the vibration $g(t)$ of the shaker. For this purpose, the trigger of the camera that marks the end of the recording is also sent to the DACQ. Both signals are simultaneously processed with a Labview interface that outputs the time delay $\Delta t \in [0, T_F/2]$ from the last recorded maximum of $g(t)$ to the end of the recording.

We then define the absolute origin of time $t = 0$ as the last maximum of $g(t)$ before impact such that the end time of the recording is given by

$$t_f = \Delta t + nT_F, \quad n \in \mathbb{Z} \tag{E 1}$$

in this reference time (figure 10). The impact time $t_i \in [0, T_F]$ is then calculated as

$$t_i = \Delta t + nT_F - (t_f - t_i) = (t_i - t_f + \Delta t)[T_F], \tag{E 2}$$

where $X[T_F]$ means X modulo T_F.

The impact phase τ_i is then

$$\tau_i = \frac{2\pi t_i}{T_F} = \frac{(\Delta t + (t_i - t_f))[T_F]}{T_F}. \tag{E 3}$$

Practically, $t_f - t_i$ is computed as a number of frames divided by the acquisition frequency.

The digital output of the DACQ is refreshed at 8 kHz, so the error on Δt is less than 0.125 ms. The impact is detected with an accuracy of (± 1 frames), which corresponds to an error on $t_f - t_i$ less than 0.25 ms. The absolute error on t_i (respectively τ_i) is then less than 0.375 ms (respectively 1.5 %).

Appendix F. Validity of the linear Navier–Stokes equations for walkers

The linear theory of Faraday waves for walkers developed in this manuscript is valid as long as the amplitude of the waves is significantly smaller than both the Faraday wavelength λ_F and the thickness of the viscous boundary layer. This latter, here denoted δ_ν, is of the order of $\sqrt{2\nu/\Omega}$. The amplitude of the wave field generated by classical walkers (oil viscosity 20 cSt, forcing frequency 80 Hz) is always less than 12 μm in the vicinity of a single walker, shortly after the impact of the droplet on

https://doi.org/10.1017/jfm.2018.358 Published online by Cambridge University Press

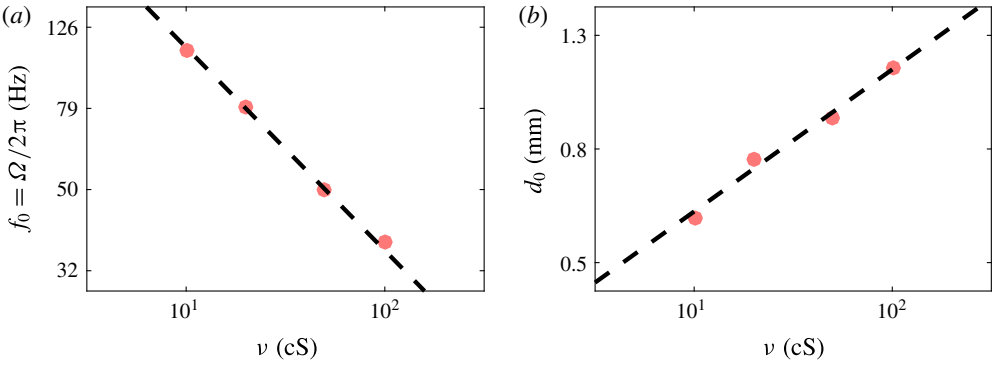


FIGURE 11. (Colour online) Data from Eddi (2011). (*a*) Log–log scaling of the evolution of the optimal forcing frequency f_0 of walkers with kinematic viscosity ν. The dashed line is corresponds to $f_0\nu^{1/2} = 3.55$ m s$^{-3/2}$ ($f_0 \propto \nu^{-1/2}$). (*b*) Log–log scaling of the evolution of the optimal diameter d_0 of walking droplets with kinematic viscosity ν. The dashed line corresponds to $d_0/\nu^{1/4} = 3.46 \times 10^{-3}$ m$^{1/2}$ s$^{1/4}$ ($d_0 \propto \nu^{1/4}$).

the bath (Damiano *et al.* 2016). This amplitude is therefore more than one order of magnitude smaller than both (i) the considered wavelength $\lambda_F \simeq 4.7$ mm and (ii) the viscous boundary layer $\delta_\nu \simeq 300$ μm. Since walkers are commonly studied below the Faraday threshold, the amplitude of their wave decreases with time, despite the forcing, so the measured 12 μm can be seen as an upper bound for the wave amplitude.

The amplitude of the waves right below the impacting droplet might be larger than the measured 12 μm on its sides. This region is challenging to observe by optical means. Nevertheless, a theoretical bound for the deflection of the bath right after impact can be obtained. This deflection mostly originates from the kinetic energy of the falling droplet. At impact, this energy is temporarily converted into surface energy, mostly associated with the bath deflection. A part of this stored energy is then restituted to the translation of the droplet (Molacek & Bush 2013), another part generates the surface wave accompanying the walker, and a last part is dissipated by viscous flows (within both the droplet and the bath) during impact. An upper bound H on the bath deflection (and on the subsequent surface waves) can be found by balancing the surface energy of the bath deflection and the kinetic energy of the incoming droplet. According to experiments (e.g. Protiere *et al.* 2006; Molacek & Bush 2013), the free fall of the droplet lasts approximately 2/3 of the bouncing period $2/f$ (where $f = \Omega/\pi$ is the forcing frequency). Consequently, the impact speed of the droplet is $v = 2g/(3f)$. To the leading order, the crater is assumed to be a spherical cap whose curvature matches half the curvature of the droplet (Gopinath & Koch 2001). The excess of surface of this spherical cap is approximately $2\pi H^2$, independently of the droplet radius. The energy balance then yields

$$H \simeq \sqrt{\frac{\rho d^3 v^2}{24\sigma}} \simeq \sqrt{\frac{\rho d^3 g^2}{54\sigma f^2}} \simeq 82 \ \mu\text{m}, \tag{F 1}$$

with a droplet diameter $d \simeq 0.8$ mm. This pessimistic upper bound H on the bath deflection, which did not take into account any dissipation or partial transfer of energy, is nevertheless again smaller than both the wavelength λ_F and the boundary layer thickness δ_ν.

https://doi.org/10.1017/jfm.2018.358 Published online by Cambridge University Press

In the discussion, we suggested that quantum-like phenomena would be likely to appear for large damping length l, i.e. for vanishing viscosity. However, the boundary layer thickness δ_ν would then decrease and could possibly become smaller than the wave amplitude, which would invalidate a description of walkers with linear waves. There have been very few experimental attempts at generating walkers with viscosity different from 20 cSt or 50 cSt (Protiere *et al.* 2005; Eddi 2011). For each viscosity in the range $\nu \in [10, 100]$ cSt, there is a narrow window of forcing frequency $f_0(\nu) \propto \nu^{-1/2}$ and droplet size $d_0(\nu) \propto \nu^{1/4}$ in which walkers could be observed (see figure 11). Substituting f_0 and d_0 in (F 1) yields $H \propto \nu^{7/8}$. On the other hand, the boundary layer thickness δ_ν would scale proportionally to $\sqrt{\nu/f_0} \propto \nu^{3/4}$. Consequently, we obtain the scaling $H/\delta \propto \nu^{1/8}$, i.e. the wave amplitude H decreases faster than the boundary layer thickness δ when the viscosity is decreased. Therefore, as far as walkers less viscous than $\nu = 20$ cSt are considered, $H \ll \delta_\nu$ and the associated Faraday waves can be described with a linear theory.

REFERENCES

ANDERSEN, A., MADSEN, J., REICHELT, C., AHL, S. R., LAUTRUP, B., ELLEGAARD, C., LEVINSEN, M. T. & BOHR, T. 2015 Double-slit experiment with single wave-driven particles and its relation to quantum mechanics. *Phys. Rev.* E **92** (1), 013006.

BECHHOEFER, J., EGO, V., MANNEVILLE, S. & JOHNSON, B. 1995 An experimental study of the onset of parametrically pumped surface waves in viscous fluids. *J. Fluid Mech.* **288**, 325–350.

BENJAMIN, T. B. & URSELL, F. 1954 The stability of the plane free surface of a liquid in vertical periodic motion. *Proc. R. Soc. Lond.* A **225**, 505–515.

BEYER, J. & FRIEDRICH, R. 1995 Faraday instability: linear analysis for viscous fluids. *Phys. Rev.* E **51** (2), 1162.

BLANCHETTE, F. 2016 Modeling the vertical motion of drops bouncing on a bounded fluid reservoir. *Phys. Fluids* **28**, 032104.

BORGHESI, C., MOUKHTAR, J., LABOUSSE, M., EDDI, A., FORT, E. & COUDER, Y. 2014 Interaction of two walkers: wave-mediated energy and force. *Phys. Rev.* E **90** (6), 063017.

DE BROGLIE, L. 1987 Interpretation of quantum mechanics by the double solution theory. *Ann. Fond. Louis de Broglie* **12** (4), 1–23.

BUSH, J. W. M. 2015 Pilot-wave hydrodynamics. *Annu. Rev. Fluid Mech.* **47**, 269–292.

BUSH, J. W. M., OZA, A. U. & MOLÁČEK, J. 2014 The wave-induced added mass of walking droplets. *J. Fluid Mech.* **755**, R7.

CARMIGNIANI, R., LAPOINTE, S., SYMON, S. & MCKEON, B. J. 2014 Influence of a local change of depth on the behavior of walking oil drops. *Exp. Therm. Fluid Sci.* **54**, 237–246.

COUDER, Y. & FORT, E. 2006 Single-particle diffraction and interference at a macroscopic scale. *Phys. Rev. Lett.* **97** (15), 154101.

COUDER, Y. & FORT, E. 2012 Probabilities and trajectories in a classical wave-particle duality. *J. Phys.: Conf. Ser.* **361**, 012001.

COUDER, Y., FORT, E., GAUTIER, C.-H. & BOUDAOUD, A. 2005*a* From bouncing to floating: noncoalescence of drops on a fluid bath. *Phys. Rev. Lett.* **94** (17), 177801.

COUDER, Y., PROTIERE, S., FORT, E. & BOUDAOUD, A. 2005*b* Walking and orbiting droplets. *Nature* **437**, 208.

DAMIANO, A. P., BRUN, P.-T., HARRIS, D. M., GALEANO-RIOS, C. A. & BUSH, J. W. M. 2016 Surface topography measurements of the bouncing droplet experiment. *Exp. Fluids* **57** (10), 163.

DUBERTRAND, R., HUBERT, M., SCHLAGHECK, P., VANDEWALLE, N., BASTIN, T. & MARTIN, J. 2016 Scattering theory of walking droplets in the presence of obstacles. *New J. Phys.* **18**, 113037.

https://doi.org/10.1017/jfm.2018.358 Published online by Cambridge University Press

DUREY, M. & MILEWSKI, P. A. 2017 Faraday wave-droplet dynamics: discrete-time analysis. *J. Fluid Mech.* **821**, 296–329.

EDDI, A 2011 Marcheurs, dualité onde-particule et mémoire de chemin. PhD thesis, Université Paris-Diderot-Paris VII.

EDDI, A., FORT, E., MOISY, F. & COUDER, Y. 2009 Unpredictable tunneling of a classical wave-particle association. *Phys. Rev. Lett.* **102** (24), 240401.

EDDI, A., MOUKHTAR, J., PERRARD, S., FORT, E. & COUDER, Y. 2012 Level splitting at macroscopic scale. *Phys. Rev. Lett.* **108** (26), 264503.

EDDI, A., SULTAN, E., MOUKHTAR, J., FORT, E., ROSSI, M. & COUDER, Y. 2011 Information stored in Faraday waves: the origin of a path memory. *J. Fluid Mech.* **674**, 433–463.

FARADAY, M. 1831 On the forms and states assumed by fluids in contact with vibrating elastic surface. *Phil. Tran. R. Soc. Lond.* **121**, 319–346.

FILOUX, B., HUBERT, M. & VANDEWALLE, N. 2015 Strings of droplets propelled by coherent waves. *Phys. Rev.* E **92**, 041004(R).

FORT, E., EDDI, A., BOUDAOUD, A., MOUKHTAR, J. & COUDER, Y. 2010 Path-memory induced quantization of classical orbits. *Proc. Natl Acad. Sci. USA* **107**, 17515–17520.

GILET, T. 2014 Dynamics and statistics of wave-particle interactions in a confined geometry. *Phys. Rev.* E **90**, 052917.

GILET, T. 2016 Quantumlike statistics of deterministic wave-particle interactions in a circular cavity. *Phys. Rev.* E **93**, 042202.

GILET, T., TERWAGNE, D., VANDEWALLE, N. & DORBOLO, S. 2008 Dynamics of a bouncing droplet onto a vertically vibrated interface. *Phys. Rev. Lett.* **100**, 167802.

GOPINATH, A. & KOCH, D. L. 2001 Dynamics of droplet rebound from a weakly deformable gas–liquid interface. *Phys. Fluids* **13** (12), 3526–3532.

HARRIS, D. M. & BUSH, J. W. M. 2014 Droplets walking in a rotating frame: from quantized orbits to multimodal statistics. *J. Fluid Mech.* **739**, 444–464.

HARRIS, D. M., MOUKHTAR, J., FORT, E., COUDER, Y. & BUSH, J. W. M. 2013 Wavelike statistics from pilot-wave dynamics in a circular corral. *Phys. Rev.* E **88**, 011001 (R).

KUMAR, K. 1996 Linear theory of Faraday instability in viscous liquids. *Proc. R. Soc. Lond.* **452**, 1113–1126.

KUMAR, K. & TUCKERMAN, L. S. 1994 Parametric instability of the interface between two fluids. *J. Fluid Mech.* **279**, 49–68.

LABOUSSE, M., OZA, A. U., PERRARD, S. & BUSH, J. W. M. 2016 Pilot-wave dynamics in a harmonic potential: quantization and stability of circular orbits. *Phys. Rev.* E **93**, 033122.

LABOUSSE, M., PERRARD, S., COUDER, Y. & FORT, E. 2014 Build-up of macroscopic eigenstates in a memory-based constrained system. *New J. Phys.* **16**, 113027.

LIOUBASHEVSKI, O., ARBELL, H. & FINEBERG, J. 1996 Dissipative solitary states in driven surface waves. *Phys. Rev. Lett.* **76** (21), 3959–3962.

MILEWSKI, P. A., GALEANO-RIOS, C. A., NACHBIN, A. & BUSH, J. W. M. 2015 Faraday pilot-wave dynamics: modelling and computation. *J. Fluid Mech.* **778**, 361–388.

MOISY, F., RABAUD, M. & SALSAC, K. 2009 A synthetic Schlieren method for the measurement of the topography of a liquid interface. *Exp. Fluids* **46** (6), 1021–1036.

MOLÁČEK, J. & BUSH, J. W. M. 2012 A quasi-static model of drop impact. *Phys. Fluids* **24** (12), 127103.

MOLACEK, J. & BUSH, J. W. M. 2013 Drop bouncing on a vibrating bath. *J. Fluid Mech.* **727**, 582–611.

MOLÁČEK, J. & BUSH, J. W. M. 2013 Drops walking on a vibrating bath: towards a hydrodynamic pilot-wave theory. *J. Fluid Mech.* **727**, 612–647.

MÜLLER, H. W., WITTMER, H., WAGNER, C., ALBERS, J. & KNORR, K. 1997 Analytic stability theory for Faraday waves and the observation of the harmonic surface response. *Phys. Rev. Lett.* **78** (12), 2357–2360.

NACHBIN, A., MILEWSKI, P. A. & BUSH, J. W. M. 2017 Tunneling with a hydrodynamic pilot-wave model. *Phys. Rev. Fluids* **2**, 034801.

https://doi.org/10.1017/jfm.2018.358 Published online by Cambridge University Press

NGUYEM THU LAM, K. D. & CAPS, H. 2011 Effect of a capillary meniscus on the Faraday instability threshold. *Eur. Phys. J.* E **34**, 112.

OZA, A. U., HARRIS, D. M., ROSALES, R. R. & BUSH, J. W. M. 2014*a* Pilot-wave dynamics in a rotating frame: on the emergence of orbital quantization. *J. Fluid Mech.* **744**, 404–429.

OZA, A. U., ROSALES, R. R. & BUSH, J. W. M. 2013 A trajectory equation for walking droplets: hydrodynamic pilot-wave theory. *J. Fluid Mech.* **737**, 552–570.

OZA, A. U., SIÉFERT, E., HARRIS, D. M., MOLÁČEK, J. & BUSH, J. W. M. 2017 Orbiting pairs of walking droplets: dynamics and stability. *Phys. Rev. Fluids* **2**, 053601.

OZA, A. U., WIND-WILLASSEN, O., HARRIS, D. M., ROSALES, R. R. & BUSH, J. W. M. 2014*b* Pilot-wave hydrodynamics in a rotating frame: exotic orbits. *Phys. Fluids* **26**, 082101.

PERRARD, S., LABOUSSE, M., FORT, E. & COUDER, Y. 2014*a* Chaos driven by interfering memory. *Phys. Rev. Lett.* **113**, 104101.

PERRARD, S., LABOUSSE, M., MISKIN, M., FORT, E. & COUDER, Y. 2014*b* Self-organization into quantized eigenstates of a classical wave-driven particle. *Nat. Commun.* **5**, 3219.

PROTIÈRE, S., BOHN, S. & COUDER, Y. 2008 Exotic orbits of two interacting wave sources. *Phys. Rev.* E **78**, 036204.

PROTIERE, S., BOUDAOUD, A. & COUDER, Y. 2006 Particle-wave association on a fluid interface. *J. Fluid Mech.* **554**, 85–108.

PROTIERE, S., COUDER, Y., FORT, E. & BOUDAOUD, A. 2005 The self-organization of capillary wave sources. *J. Phys.: Condens. Matter* **17** (45), S3529.

PUCCI, G., HARRIS, D. M., FARIA, L. M. & BUSH, J. W. M. 2018 Walking droplets interacting with single and double slits. *J. Fluid Mech.* **835**, 1136–1156.

PUCCI, G., SÁENZ, P. J., FARIA, L. M. & BUSH, J. W. M. 2016 Non-specular reflection of walking droplets. *J. Fluid Mech.* **804**, R3.

SAMPARA, N. & GILET, T. 2016 Two-frequency forcing of droplet rebounds on a liquid bath. *Phys. Rev.* E **94**, 053112.

TAMBASCO, L. D., HARRIS, D. M., OZA, A. U., ROSALES, R. R. & BUSH, J. W. M. 2016 The onset of chaos in orbital pilot-wave dynamics. *Chaos* **26**, 103107.

WAGNER, C., MÜLLER, H.-W. & KNORR, K. 2003 Pattern formation at the bicritical point of the Faraday instability. *Phys. Rev.* E **68**, 066204.

https://doi.org/10.1017/jfm.2018.358 Published online by Cambridge University Press